CHARACTERIZATION OF NANOCRYSTAL-BASED PHOTOVOLTAICS: ELECTRON MICROSCOPY & ELECTRON BEAM-INDUCED CURRENT VIA SCANNING ELECTRON MICROSCOPY

By

Amy Ng

Dissertation

Submitted to the Faculty of the

Graduate School of Vanderbilt University

in partial fulfillment of the requirements

for the degree of

DOCTOR OF PHILOSOPHY

in

Chemistry

May, 2015

Nashville, TN

Approved:

Professor Sandra J. Rosenthal

Professor David E. Cliffel

Professor Charles M. Lukehart

Professor Stephen J. Pennycook

Dedicated to

all my family and friends who never gave up on me

ACKNOWLEDGEMENTS

I would like to thank my committee Drs. Sandra Rosenthal, David Cliffel, Charles Lukehart, and Stephen Pennycook for all their persistence to keep my research and understanding of the work top-notch. I would like to give my greatest thanks to Sandy, who inspired me to keep pushing forward despite all the obstacles and for giving me the opportunity to explore a realm of science I never imagined I would ever be able to study. And thank you, Steve, for all your advice and encouragement.

First, I would like to acknowledge my funding: NSF TN EPSCoR (grant EPS-1004083) as well as the U.S. Department of Energy, Office of Basic Energy Sciences, and ORNL's Center for Nanophase Materials Sciences for instrument use.

For all the people who have contributed to furthering my knowledge and growth as a scientist and person. James: thank you for teaching me the TEM and being the group encyclopedia. You opened the door to electron microscopy and that is one of the most significant things that has happened to me. Your guidance is not overlooked. To all the VINSE staff (Tony, Ben, Bo) for coming to the rescue when something went wrong, your help through the years is immensely appreciated. Nat, your open demeanor as well as advice and help with devices have been endless – thank you! Joyce and John D.: thank you both for being so patient with me while I fiddled around with the FIBs. Sarah S. and Pat T., it's always so nice to see your smiling faces after a long day's work; I will miss you both!

To my lab family past and present at Vanderbilt: thank you for all the beautiful memories. From the 9th floor floods to group lunches, there are far too many moments to name. Sarah, it was one of the saddest days when you left the lab, but I am so glad we have continued to meet up and have "dates." To know how well you're doing now is truly one of the best feelings – you deserve it! We've helped each other through so much, and I'm so very happy to be able to call you a friend. Jerry, you are living proof that hard work and perseverance pay off in big ways. Thank you for your encouragement and time. Toshia, Oleg, Melissa, Joe, Noah, Scott, Albert, Xochitl: thank you all! No matter where the future takes us, you are my academic siblings for whom I am always grateful to have.

My Oak Ridge colleagues and friends: thank you for everything. There are too many people to name individually; so many of you have contributed to my (sanity and) successes. It has been a pleasure to have met, worked, and partied with you. Donovan, you have been a great support and help throughout my graduate career. It was a pleasure to work alongside such an intelligent and patient person. Thank you for all the guidance – I would not have made it this far without you. Jon, your hard work on the EBIC project has not been for naught; thanks for helping me to graduate!

I am fortunate enough to have so many people to call family, but last and certainly not least, is family back home who cheered me on through thick and thin. Mom and Dad, your unconditional love for me and my dreams has allowed me to grow into a person who not only loves her work but also loves those who stand silently by

wishing me all the best. Mason, you've been the best big brother; if it weren't for your support, I would not have chosen this path academically. Thank you; I hope that, as a little sister, I have made you proud. Mama and grandpa, thank you for your endless love. Eleni, Matt, Morgan, Tram, and Courtney, all your love and support has led me to this moment. It would only be appropriate to return all of that and more! I'll be back.

Last but not least, Matt, my friend and other half: words cannot comprehend how much you mean to me. Thank you for all your care through graduate school and life in general – your visits and texts kept me from losing my mind on a regular basis. I finally made it!

TABLE OF CONTENTS

LIST OF TABLES

LIST OF FIGURES

LIST OF ABBREVIATIONS

AFM ……. Atomic force microscopy

DDPA ……. Dodecylphosphonic acid

EBIC …… Electron beam-induced current

EDS …… Energy dispersive spectroscopy

FTO ……..Fluorine tin oxide

HAADF ……High angle annular dark field

IBID …….. Ion beam induced deposition

ITO ……. Indium tin oxide

MEMS …….. Microelectromechanical system

NMP ……. 1-methyl-2-pyrrolidinone

ODE ……. Octadecene

P3HT…….. Poly-3(hexylthiophene)

PCE……Power conversion efficiency

PEDOT:PSS …… Poly(3,4-ethylenedioxythiophene):poly(styrenesulfonate)

PV ……. Photovoltaic

SEM …….. Scanning electron microscope

STEM ……. Scanning transmission electron microscope

TBP …….. Tri-n-butylphosphine

TCB …….. 1,2,4-trichlorobenzene

TCO……Transparent conductive oxide

TEM ……Transmission electron microscope

TOPO ……. N-tri-octylphosphine oxide

CHAPTER I

INTRODUCTION

World-wide energy consumption has reached staggering numbers: 511 quadrillion btu was used in 2010 alone.[1] With an ever-increasing population and industrialization, the demands will only become greater in the future. In order to meet these needs and reduce greenhouse gas emissions, alternative forms of energy must be further explored. The most abundant sources is sunlight; based on the solar constant, thirty minutes of direct sunlight on an area the size of the Vanderbilt University campus can provide enough energy for an average person in the United States for ten years![2]

In order to harness this potential, research to develop new technologies and improve established photovoltaic (PV) devices, such as single crystalline silicon, is highly prevalent. Most technologies such as Si-based ones are very costly to manufacture (i.e. thick samples, extreme conditions) and therefore have repressed the widespread use of PVs.[3] Until recently, few consumers could afford to have a solar panel installed on a building, etc. The advent of second generation PVs, for instance, CdTe or CIGS thin films, was explored due to this.[3,4] As of 2013, this form of PV has reached 21.7 % laboratory efficiency.

One of the most promising designs for a low cost and high theoretical efficiency PV device incorporates nanoscale components such as colloidal nanocrystals (see Section 1.1).[5] These devices possess greater active area due to the fact that each

nanocrystal, at less than 100 nm, acts as a p-n junction (Section 1.2); their theoretical efficiency reaches over 60%, double that of silicon and other thin film technologies (at about 30%).[3,6] Then why, one may ask, have these PVs not dominated the solar cell market? There are numerous obstacles inhibiting the full potential of these types of PVs, mainly in the synthetic and fabrication routes. Colloidal nanocrystals are synthesized with organic, insulating ligands on their surface, which prevent the electron and hole from separating readily, hence the less than ideal power generation. Moreover, there are far more interfaces to take into consideration than for thin film PVs; for example, the nanocrystals contacting one another and the contact of those nanocrystals to the cathode and/or anode. The probability that there are additional inhibiting factors such as creating a balance between device architecture and parameters such as shunt resistance, causes more discrepancy, thus more difficulty in elucidating concrete reasons as to why these devices suffer from poor efficiencies.

Interfacial studies at the nanoscale are necessary for PV device development; whether every active region is making the appropriate contacts for charge flow becomes critical for the overall architecture. Thin film materials, such as $Cu(In,Ga)Se_2$, have been investigated in such a manner, where phase analysis, planar defects, and charge carrier collection can be determined from simultaneous structural and electronic imaging.[7] Due to the size regime of the nanocrystal-based devices, conventional instrumentation is helpful but insufficient. Without a better understanding of the technology, improvements cannot be made.

The work in this thesis demonstrates, for the first time, a combination of near-atomic resolution electron micrographs correlated with electronic activity maps for a nanocrystal-based PV. The methodology employed will assist in determining the deficiencies of these nanocrystal-based devices and providing insightful information regarding their electronic pathways. As a result of these findings, the appropriate steps for improving the technology will aid in the advancement of the field; additionally, the next generation of solar cells would be on the horizon with the discoveries.

1.1 Semiconductor Nanocrystals

Semiconductor nanocrystals are single crystalline material exhibiting a property called quantum confinement, which is an effect that results in the nanoscale material behaving differently than its bulk counterpart. Quantum confinement allows the optical properties to be controlled by adjusting the diameter of the nanocrystal, making them highly beneficial toward applications in LEDs,[8–11] biological markers,[12,13] laser diodes,[14] quantum computing,[15,16] catalysis,[17,18] and photovoltaics.[19–21] Briefly, the nanocrystal is small enough so that their electron-hole pair (EHP), or exciton, is much less than that of the Bohr exciton radius of the bulk material, thus forcing the EHP to be closer. The energy gap between the valence and conduction bands increases with the decrease in size of the nanocrystal. The energy, when a photon excites the electron from the valence band, given off from the relaxation of the electron from the conduction band back to the valence band releases a specific wavelength of light inversely proportional to that of the band gap. This particular property is ideal for fluorescence studies.[12,22]

However, for solar cells, the most imperative step in the functionality of the nanocrystal lies in the electron excitation to the conduction band and then extraction, allowing it to be swept into an external circuit thus producing electricity. A more in depth discussion of the mechanism of photovoltaics is in Section 1.2.

Nanocrystals can be composed of various materials including but not limited to Cd, Se, S, Te, Pb, Cu, In, Zn, and Ga.[19,23] Depending upon the application, certain combinations will yield more appropriate outcomes than others; for instance, solar cells would benefit from materials that absorb as much of the solar spectrum as possible (Figure 1.1). The example used in Figure 1.1 is the comparison of the II-VI nanocrystal, CdSe to the solar spectrum, where in Section 1.2.1, further explanation of the architecture of the device is discussed.

1.2 Photovoltaics

A semiconductor material that is able to convert light energy to direct current electricity is referred to as a photovoltaic. Its ability derives from the built-in potential found inherently in the design of the device. A typical photovoltaic, such as those found commercially, operates upon the premise that there are two sides – a net positively charged side (p-doped) and predominantly negative side (n-doped). As shown in Figure 1.2, there exists an area interfacing both sides, also known as the space charge region, or depletion region. This area is the origin of EHPs, and the charges soon after generation, become separated by diffusion. These minority charge carriers migrate to their respective electrodes and then to an external load.

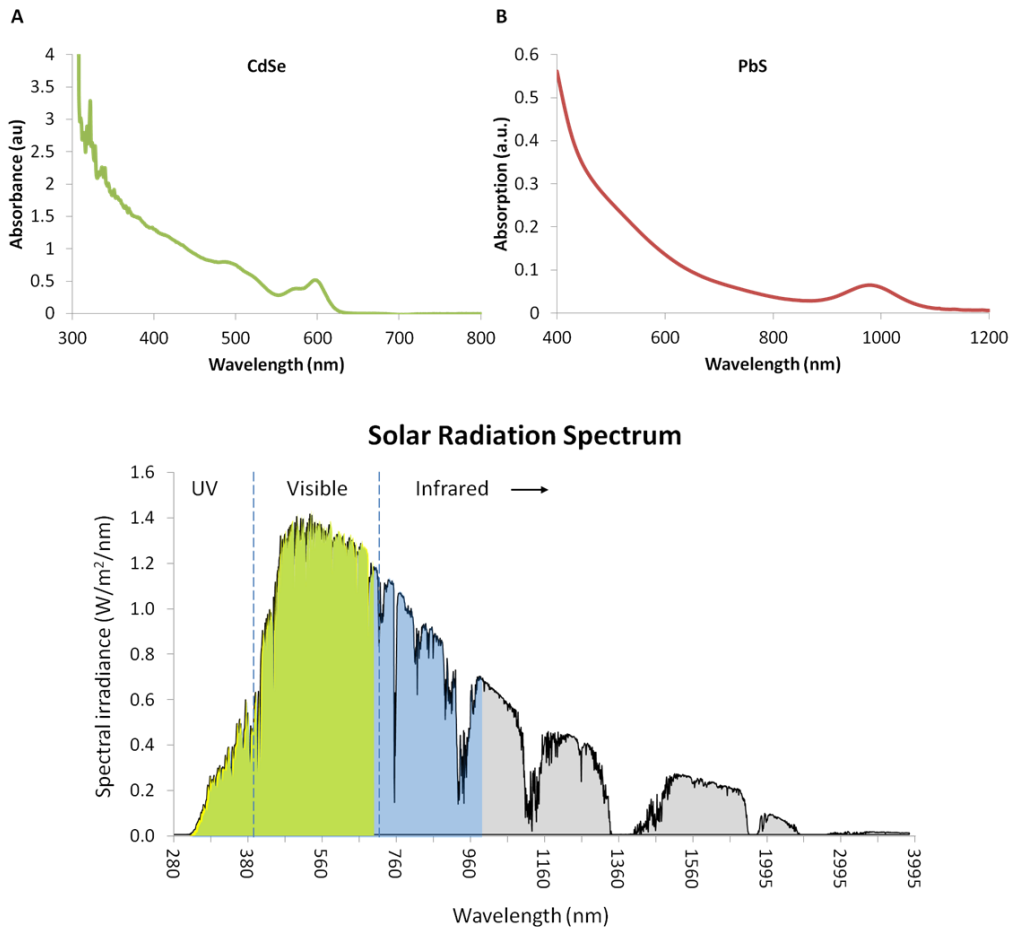

Figure 1.1 (A) and (B) show the absorption spectra of CdSe and PbS, respectively. Highlighted in green on the solar radiation spectrum is CdSe, and regions of both green and blue are where PbS absorbs.

The most common form of this photovoltaic, or solar cell, is a commercially available silicon device with an efficiency of about 10 %. Although not a staggering value, this efficiency is at least one third of its theoretical maximum of about 30%. Other forms of photovoltaic technologies, such as that of nanocrystal-based photovoltaics, remain at insubstantial efficiency values, especially compared to their theoretical efficiencies (approximately 65%);[24] the most recent achievement was made by Chuang et al with a certified efficiency of 8.55%.[25]

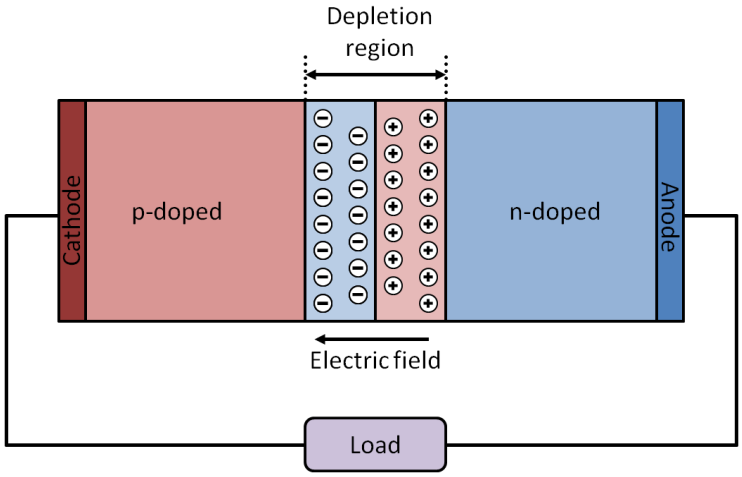

Figure 1.2 A generic schematic of a traditional solar cell.

The different components that impact this "efficiency" (the ratio of power output and power input) can be described by a factor termed external quantum efficiency (EQE, where it is the ratio of charge carriers collected and photons striking the solar cell). Equation 1.1 and Figure 1.3, for a polymer and inorganic acceptor device (CdSe:P3HT device), breaks down the roles of charge transfer.

$$EQE = \eta_a \times \eta_{ex} \times \eta_{diff} \times \eta_{diss} \times \eta_{tr} \times \eta_{cc} \quad (1.1)$$

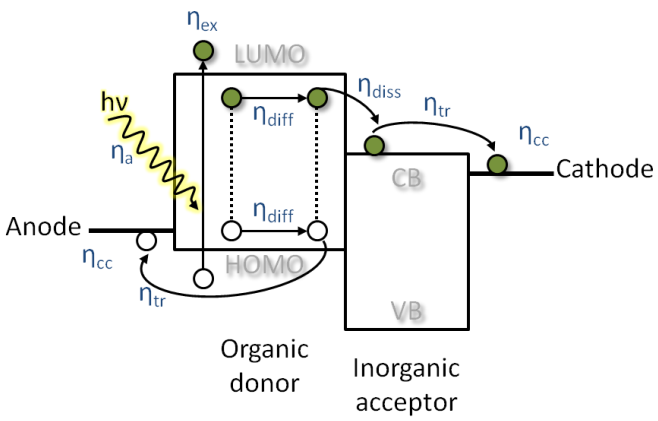

Figure 1.3 Charge transport diagram for an organic/inorganic photovoltaic system.

The factor η_a corresponds to the photon absorption, which is dependent on the optical absorption and thickness of the photoactive layer. The exciton generation, η_{ex}, is simply the excitation of the electron from the valence band to the conduction band (lowest unoccupied molecular orbital or LUMO) leaving a hole in the highest occupied molecular orbital (HOMO). As these electrons and holes diffuse (η_{diff}) through the polymer, some would dissociate (η_{diss}) by the internal electric field at the heterojunction. Once the charge successfully dissociates, the ability of the electron (also true for the hole) to transfer to the cathode is summed up in the factor η_{tr}. Lastly, the collection of the charges at their respective electrodes is represented by η_{cc}. All these yields contribute to the EQE; if any of these are near zero, the entire device efficiency would be affected.

While efficiencies and the factors that impact it, e.g. open circuit voltage, short circuit current, etc., reveal a great deal about a solar cell, there are limitations to this macroscopic form of measurement. Especially with the architectures studied in this

work, looking at a value has little meaning when the problems lie at a different magnitude of length scale. In order to make improvements to the technology, the ability to observe the effects of structural changes at the micro- and nano- length scales is necessary.

1.2.1 Architectures of interest

1.2.1.1 CdSe:P3HT

The primary architecture studied is a hybrid inorganic, organic device. The inorganic component is CdSe nanorods, while the organic is poly-3(hexylthiophene), or P3HT; they serve as the electron acceptor and electron donor, respectively. The architecture is referred to as a bulk heterojunction (BHJ) due to the fact that it is a bicontinuous solid dispersion, where the interspersed materials possess semiconductor properties.[26]

One of the reasons why this type of device has potential is that charge transfer is favored between high electron affinity inorganic semiconductors and relatively low ionization potential organic polymers.[27] In addition, the ability of each nanocrystal forming an EHP significantly increases the probability of current generation compared to a single-crystalline solar cell; this is also true of all nanocrystal/quantum dot-based devices. The cost of fabricating such devices is also significantly reduced because of the, for example, enhanced absorption coefficient of nanocrystals, where a small amount of active material can generate an equivalent number of EHPs as much thicker materials.[27] Colloidally synthesized nanocrystals also decrease the cost of fabrication due to the ease

of processing via solubility of the material; therefore a variety of routes can be taken for deposition onto an appropriate surface.

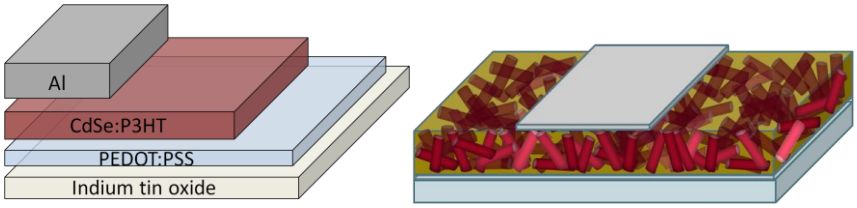

Figure 1.4 CdSe:P3HT device.

The basic components of the device are as follows from the bottom up: (1) glass coated with indium tin oxide (ITO) serving as the hole conductor/anode, (2) PEDOT:PSS is the electron blocking layer as well as the smoothening agent for the often rough surfaced ITO, (3) blend of pyridine-capped CdSe nanorods and P3HT at a 9:1 ratio as the photoactive layer, and (4) Al caps the device as the cathode (Figure 1.4). The rods, in particular, play one of the most crucial roles in the device, as they have the ability to direct charge flow as well as reduce the number of hopping steps for electron extraction in comparison to spherical particles.[27,28] In the case of the former, charge flow is directed due to the confinement of the nanorods in one direction. Additionally, the aspect ratios can be adjusted so as to absorb an ideal amount of incident light.[27,29,30] Also notable is the pyridine ligand at the surface of the rod which assists to augment the

conductivity of the film.[31] The low electronic barrier in comparison with TOPO allows the electron transport to be less inhibited by insulating ligands.

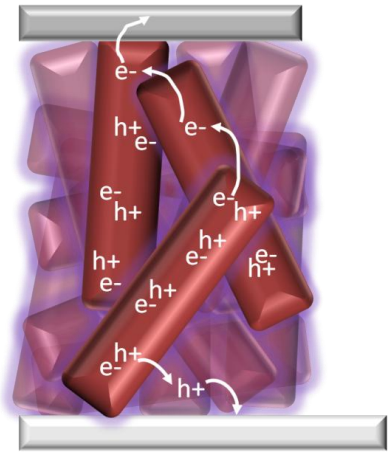

Figure 1.5 Mechanism of charge transport for CdSe:P3HT device.

The mechanism behind the functionality of this device is believed to be consisting of numerous hopping steps, as depicted in Figure 1.5. The hole from the rod behaves similarly, however the hole is transported to the polymer and then captured at the ITO. Since the P3HT is an electron donor, its electron is given to the nanorod, while the hole travels to the ITO to be extracted. The electrons have a moderately more complex route as they must percolate from nanocrystal to nanocrystal in order to arrive at the Al cathode. While bulk CdSe has an electron mobility of 660 $cm^2V^{-1}s^{-1}$, it is severely limited by the hopping mechanism between nanocrystals; P3HT, on the other

hand, has a hole mobility of 0.1 $cm^2V^{-1}s^{-1}$ suggesting that it does not possess strong transport properties.

1.2.1.2 PbS depleted-heterojunction

This quantum dot depleted-heterojunction architecture was first introduced by the collaboration of Edward Sargent (University of Toronto) and Michael Grätzel (École Polytechnique Fédérale de Lausanne), where the initial efficiencies were approximately 3%.[32] Over several years, the PCE increased to 8.5% with modifications to the original device. The basic premise behind this device structure is the mimicry of a thin film as well as a dye sensitized solar cell. As shown in Figure 1.6, a loosely packed TiO_2 particulate layer is coated onto an FTO glass slide; above that is several coats of 3-mercaptopropionic acid-capped PbS quantum dots are sandwiched by a metal contact (for the devices in this work, it is Au and then Ag). This device relies heavily on the fact that the layers are of a particular thickness to achieve complete depletion throughout the active region.

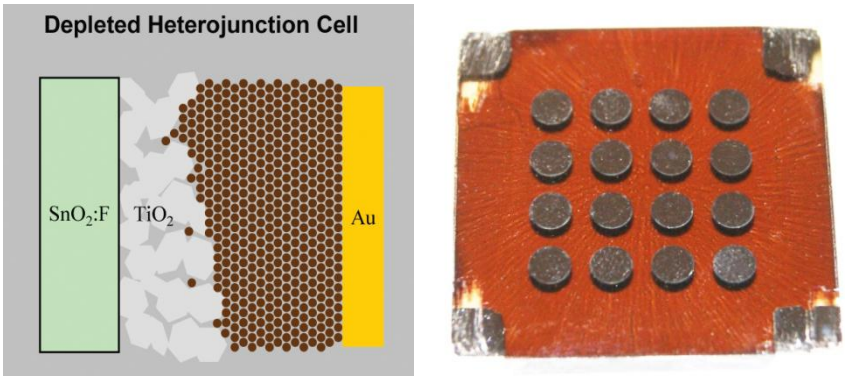

Figure 1.6 PbS depleted heterojunction solar cell. From Pattantyus (left) and Sargent group (right).

As one of the most successful device designs to date for quantum dot-based photovoltaics, it is one of the most promising architectures for further studies. With the methods shown here (Chapter IV), improvements to the overall performance were achieved in comparison to a pristine (fabrication of an as-described published device) solar cell. Other means of optimization were conducted by the Sargent and Bawendi groups.[25,33–36]

1.2.1.3 TiO_2 nanotubes

Tubular TiO_2 structures improve upon the traditional Grätzel cell architecture by increasing the surface area. Past studies used the nanotube design for dye-sensitized devices;[37–39] however, the application of nanocrystals to this structure is not well researched.[40,41] By implementing quantum dots, in this case PbS, the charges generated at each nanocrystal separate, where the electrons flow through the nanotubes as the holes are funneled through the ITO (Figure 1.7).[42]

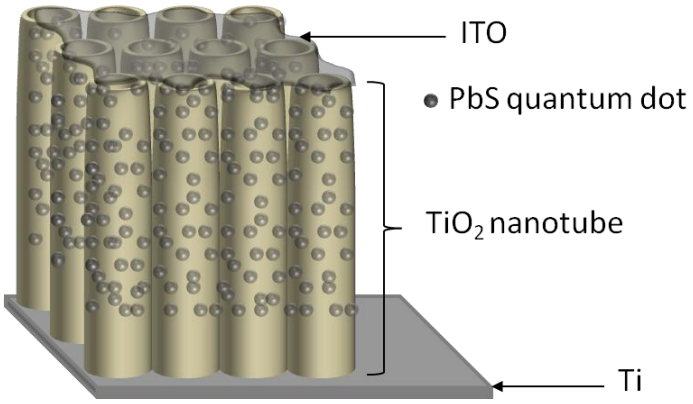

Figure 1.7 PbS quantum dot sensitized TiO_2 nanotube architecture.

The means and efficiency of introducing the nanocrystals into the tubes is critical for overall device performance. For the fabrication of titania nanotubes, anodization of Ti foil with an ethylene glycol ammonium fluoride-based solution is performed under a potential bias of 40 V for two hours. These 20 µm long tubes have an inner diameter of approximately 50 nm and are organized in a hexagonal array.[43,44] The PbS nanocrystals are deposited via a successive ionic layer adsorption and reaction method, and the electron-beam evaporated ITO was layered using the Angstrom system in VINSE.[42]

1.3 Transmission Electron Microscope (TEM)

Until Louis de Broglie discovered the relationship between the energy and the wavelength of an electron, magnification was limited to light-based microscopy. The first electron microscope was built several years prior to this finding; the microscope at the time, had a resolution that was comparable to that of a light-based one, but its potential was far greater when modifications were made.

In order to better understand why an electron is used for microscopy, one must realize resolution limitations. Equation 1.2 represents the resolution limits of the smallest distance between two objects:

$$\delta = \frac{0.61\lambda}{\mu \sin\beta} \tag{1.2}$$

where λ is the wavelength of radiation, μ the refractive index of the viewing medium, and β the semi-angle of collection of the magnifying lens. For a light microscope, the maximum resolution determined by the equation is about 330 nm of a 550 nm wavelength of light assuming the denominator is approximately equal to unity. With an electron at an accelerating voltage of 100 keV, on the other hand, the calculated resolution is approximately 2 pm, significantly less than the diameter of an atom.[45]

De Broglie's discovery of the duality of an electron (wave vs. particle) plays a significant role as to why the electron works for microscopic purposes. Due to the fact that the incident beam can behave as a particle, electron scattering can take place, e.g. inelastic scattering.[45,46] On the other hand, diffraction also relies on the fact that electrons can take on a wave nature.

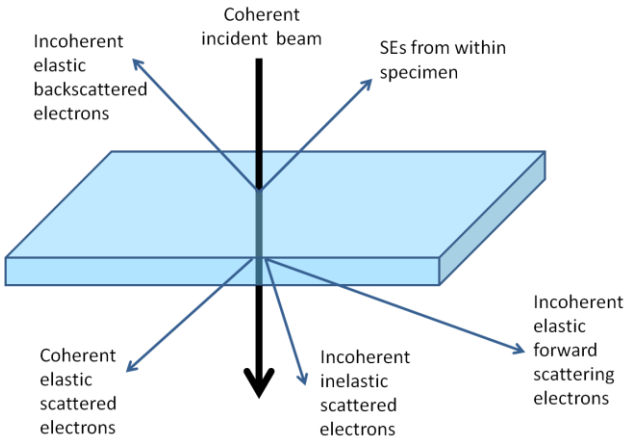

Figure 1.8 Incident beam interactions in a thin specimen.

With TEM, there are numerous potential interactions the coherent incident electron beam can have on a thin specimen. As shown in Figure 1.8, there are several primary categories: coherent vs. incoherent (wave nature), elastic vs. inelastic (particle nature). Using these electron-specimen interactions, different types of data can be extrapolated; this includes diffraction patterns, spectra (electron energy loss or energy dispersive), and, of course, bright field or dark field images.

For a traditional TEM, specimens are typically imaged using a parallel beam. Originating from an electron source (e.g. LaB_6 thermionic source for the VINSE Philips CM20), electrons travel downward following a vertical optic axis. Starting from the gun crossover, the electron spread passes through the first condenser lens which results in crossover again. Once again, the beam spreads but as it passes through the second condenser aperture, the electrons' angular extent is controlled, and then pass through

the objective aperture to the specimen. An image of the sample is then projected onto a screen.

Significant disadvantages to TEM include the necessity of imaging thin specimens and small sample size. During the preparation of such samples, damage can be inflicted to the specimen, both structurally and chemically.[45] Moreover, the size of the specimen is quite limited (~3 mm discs) in comparison with what can be achieved with light microscopy or even scanning electron microscopy. In addition to the thin specimen preparation factor, interpretation of the micrographs can become difficult because of the inadvertent damage from both the aforementioned and beam induced, etc. However, over the years, microscopists have learned to distinguish artifacts from actual sample-related features.

A powerful tool for high magnification and diffraction analyses, TEM is a great compliment to other techniques, but it alone can impart tremendous amounts of information if utilized effectively. With an emphasis on crystalline materials, a TEM can provide information including but not limited to crystal structure in addition to various kinds of spectral data. TEM is primarily used as a tool to measure the aspect ratios of synthesized nanocrystals in this document.

1.4 Scanning Electron Microscope (SEM)

Scanning electron microscopy, one of the primary techniques used in this work, relies upon a means of rastering the coherent electron beam over the surface of a specimen. The accelerating voltage of an SEM, compared to that of a conventional TEM

has an approximate two magnitude difference; the typical operating voltage of the experiments presented here are about 5 kV. This beam is focused by condenser lenses, which then either passes through scanning coils or deflector plates so that the beam can "move" in the x and y directions.

As an electron beam scans across the sample, four primary types of signals are detected: secondary (SE), backscattered (BSE), cathodoluminescence (CL), and X-rays (Figure 1.9). SEs assist in morphological and topographical detection, while BSEs primarily are utilized for atomic number contrast for compositional discrepancies. Optical properties of a sample are registered by CL. X-rays, based on the interactions between the electrons in the discrete orbitals of the atom, produce elemental information of a specimen; this spectroscopic method is known as energy dispersive x-ray spectroscopy, or EDS. These individual signals are then collected by their respective detectors and translated from an analog signal to a digital one yielding a grayscale image on a computer screen.

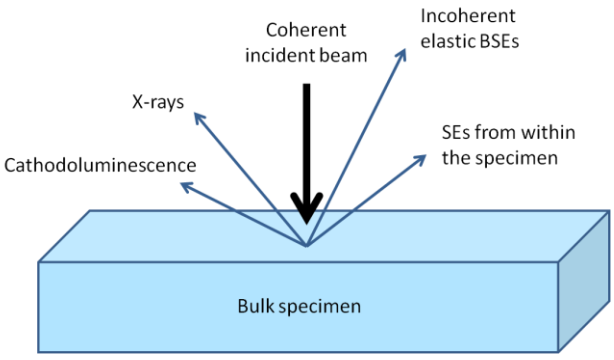

Figure 1.9 Incident beam interactions with a bulk/thick specimen.

Despite utilizing electrons to magnify objects, TEM and SEM are different. All the SEMs (Tescan Lyra3 and Zeiss Auriga FIB/SEM and Hitachi S4800) presented in this thesis are field emission gun (FEG) equipped for electron generation. Unlike TEM, the magnification of an SEM is controlled by the current supplied to scanning coils or voltage to the deflector plates rather than the projector lenses.

There are, however, drawbacks to SEM, including limited resolution, due to the spot size and interaction volume of the electron beam. The positive aspects, however, outweigh the negatives depending on the goal of the user: (1) entire samples can be analyzed without tedious preparation, (2) topographical imaging is ideal with SEM, (3) wide range of signals able to be detected for multiple analyses, and (4) objects appear in a somewhat 3D manner due to the large depth of field.

1.5 Scanning Transmission Electron Microscope (STEM)

STEM is a combination of components from SEM and TEM as the name implies. With this instrument, it takes into account the lateral resolution limitations of SEM and the imaging lens dependence shortcoming of TEM and improves on them.[45] With TEM, typically a parallel beam is used, but in a similar manner of condensing the beam, a convergent beam of electrons is formed (probe) for STEM (Figure 1.10A). Compared to SEM, STEM reduces the interaction volume through its use of thin samples; a higher energy electron beam also helps to reduce the lateral beam spreading (Figure 1.11).[47] This is particularly ideal for EBIC (Chapter VI) as will be discussed later. Furthermore,

various modes of imaging, scanning, and diffracting from TEM and SEM can be used for STEM.

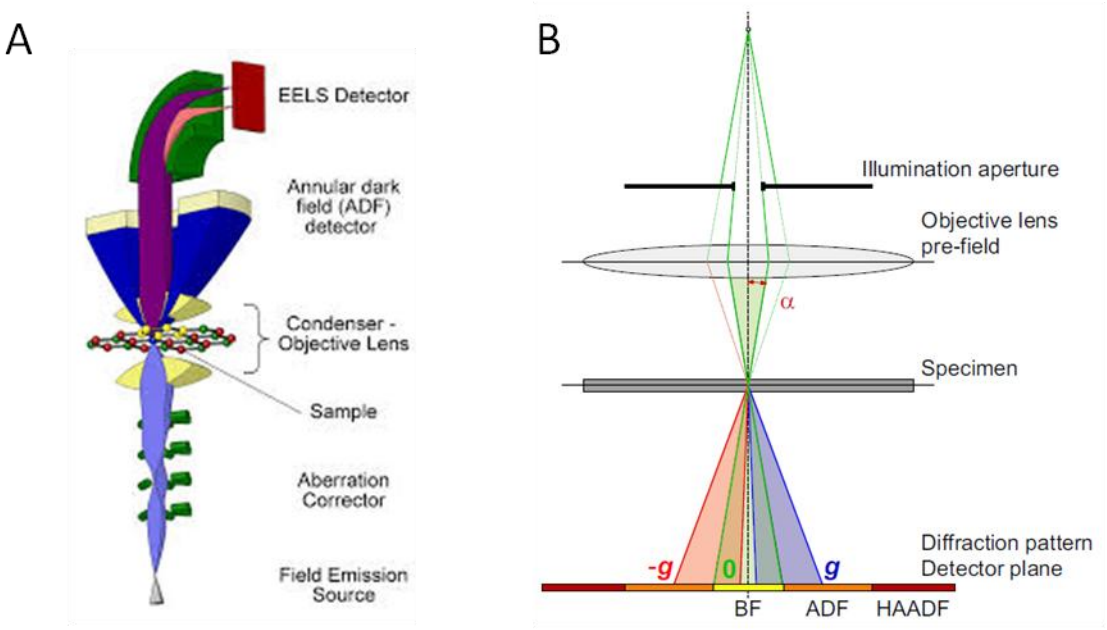

Figure 1.10 (A) STEM with aberration correction schematic and (B) STEM imaging modes based on angles of collection.[48]

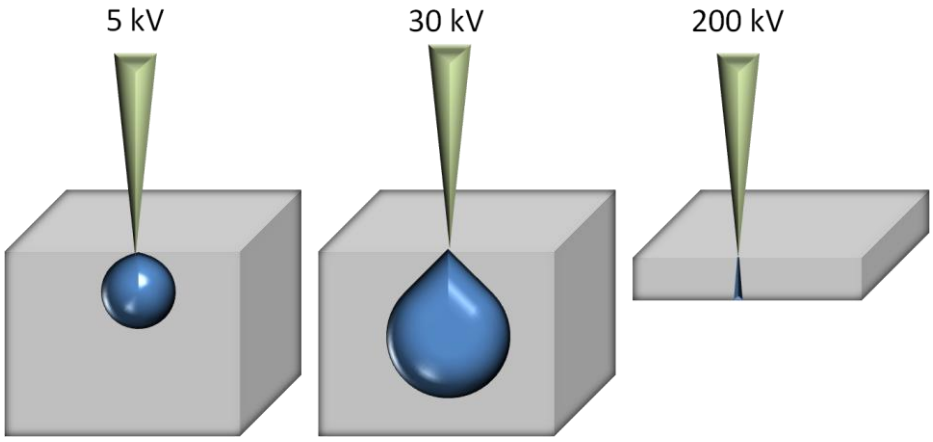

Figure 1.11 Interaction volume vs. accelerating voltage vs. sample thickness.[47]

There are several forms of imaging on a STEM, for example, the most used, high angle annular dark field (HAADF) as shown in Figure 1.10B. Based upon the electron scattering angles, different kinds of information can be collected; while using HAADF for instance, one is able to comparatively observe the atomic number of an atom. The resolution of STEM is limited by the probe diameter, thus the next section becomes very important for the improvement of the technology's resolution.

1.5.1 Spherical aberrations

There are two major forms of aberrations that affect the resolution of electron microscopes: spherical and chromatic. The latter relates to the frequency, wavelength or energy of the electrons, while the former occurs when the lens field behaves differently for off-axis rays. Spherical aberrations yield blurred images due to the concavity of a lens. For instance, the electrons that strike the outer portion of a lens will deflect differently than the ones toward the center, namely, the ones at the center will be focused at one point, while the others will be focused elsewhere along the optical axis.[45,48]

The STEM used for some of the work in this document is a Nion UltraSTEM 200, a probe-corrected microscope (Cs-STEM). This instrument utilizes several quadrupole and octupole electromagnetic lenses coupled with computer software to lessen the effects of those aberrations.[49] An algorithm is run while a recording of amorphous carbon Ronchigrams are collected; cross-correlation of the images yields an aberration-corrected probe, which would then assist in producing "cleaner" micrographs.[48] As

shown in Figure 1.12A and C, spherical aberration causes a beam to broaden at the sample, while a corrected situation, B, produces a finely focused beam. STEM benefitted greatly from the development of aberration correction; it helped to increase the resolution by a factor of two by generating a smaller electron probe with higher currents.[45,50]

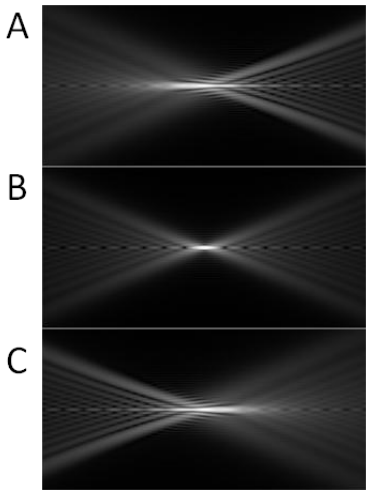

Figure 1.12 Spherical aberrations, (A) negative and (C) positive, and (B) aberration-corrected cases where the lens is at the left. Shown are the longitudinal sections through a focused beam.

1.6 Focused Ion Beam (FIB)

Similar to electron microscopy, focused ion beam (FIB) utilizes a focused beam of ions, rather than electrons. The principle of FIB is simple: focused ions ablate or assist in depositing onto a specimen surface.[51] There are numerous applications for FIB in industry, including lithography for integrated circuit fabrication and repair.[51,52] An

example of what the sample chamber of a dual beam FIB is shown in Figure 1.13. In addition to the FIB components, a dual beam FIB also incorporates an SEM to image while making FIB cuts and deposits. One of the significant benefits of this system is the ability to manipulate ion sensitive samples.

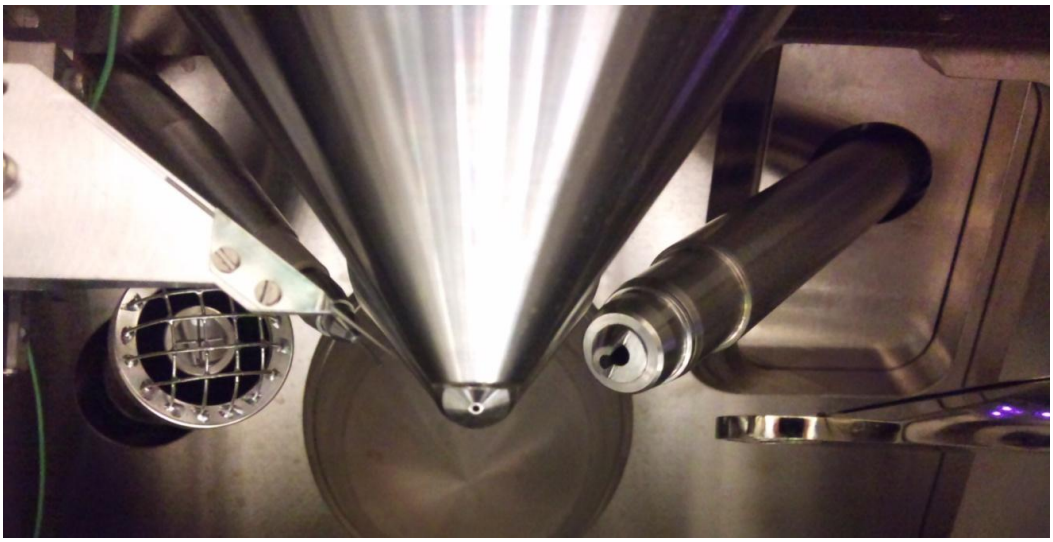

Figure 1.13 The chamber of the Tescan Lyra3 at Middle Tennessee State University.

The general steps to the mechanics of a Ga^+ ion FIB are described below. Gallium is one of the most common types of ion source for FIBs. By inducing a voltage through liquid Ga, a sharp tip forms from a Taylor cone; this tip generates ions that are then focused to as narrow as 5 nm by electrostatic and surface tension forces, which becomes beneficial for site specific applications.[53–55] The Ga^+ ion is then accelerated via a potential down the column, where it passes through two lenses: condenser and

objective. The condenser lens forms the probe, and the objective focuses the beam. Apertures are also present to adjust the probe size as well as controlling the beam currents (ranging from pA to nA), where the latter significantly affects the ability of the ion beam to perform certain tasks, such as TEM lift outs. Lastly, there is a beam blanker to deflect the beam away from the center of the column.

Voltage, similar to EM, can be adjusted depending upon how it will be used. For imaging, lower kilovolt voltages are used for a more disperse ion beam; higher voltages are used for etching or depositing. As important as the voltage is, another factor to take into consideration is the measured probe current. Based on the voltage and apertures used, different probe currents can be achieved. For faster, coarse milling, high probe currents (e.g. 2 nA) are utilized; fine polishing and depositing use smaller values (e.g. 100 pA or less).

The concept of using ions to etch and/or deposit materials is one that was developed in the 1970's. Etching is simpler to understand as it takes advantage of the density and momentum of an ion – incoming ions would sputter off pieces of the sample at a controlled rate (Figure 1.14). When an ion transfers enough energy to the sample that it overcomes the surface binding energy of the target, the sputtering phenomenon occurs. Sometimes, an etchant gas is also used to assist in this process. In that case, the etchant binds to the surface of the sample and forms a volatile complex which is pulled into vacuum. Again, the focused nature of the ion beam becomes significant due to the fact that the areas of where the sample is milled are isolated to a precise region.

Deposition, on the other hand, is slightly more complex as it requires a gaseous precursor material, e.g. tungsten hexacarbonyl for tungsten, phenanthrene for carbon, tetrakis(trifluorophosphine)platinum for platinum, etc.[56,57] This gas is injected through a gas injection system (GIS) needle situated very close to the sample surface. Simultaneously, ions bombard the specimen as the gaseous complex is introduced. The metal precursor adsorbs to the specimen, while the remainder of the molecule becomes a volatile species due to the ions and is whisked into vacuum. A common and relevant use for the FIB includes TEM specimen preparation. What is called the "lift-out" method is described in more detail in Sections 2.5.2 and 2.5.3.[58] This preparation step produces an electron transparent cross-section of the sample that then permits the analysis of a full depth view, which may include sample defects.

One of the major drawbacks of FIB is inadvertent damage from the ion beam that can range from sample heating to nonspecific/excessive sputtering as well as undesirable deposition, i.e. redeposition. In particular, because ions are dense, they tend to embed themselves into the specimen. The implantation can produce an amorphous material at the sample surface or interact with the sample forming Ga metal species. The latter would be impossible to prevent, so FIB would not be the appropriate technique for sample preparation; however, the former's effects can again be lessened by low probe current polishing.[55]

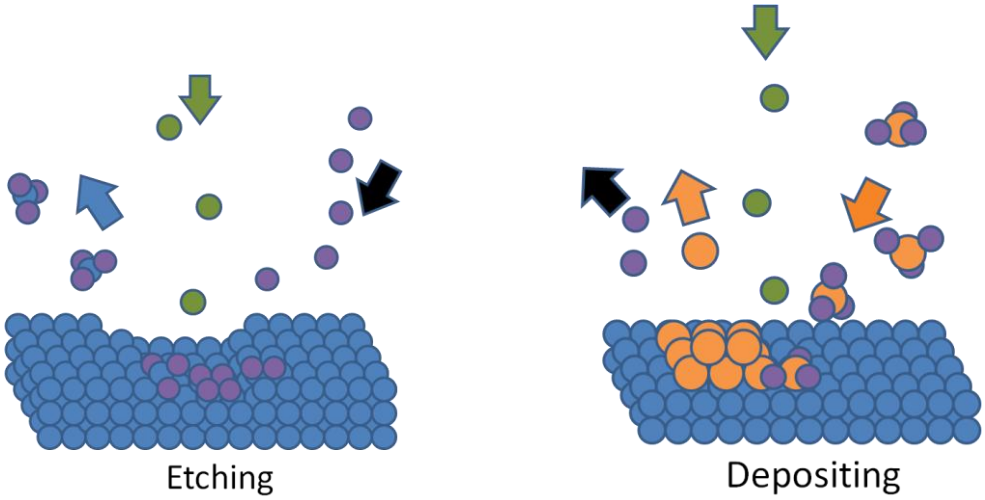

Figure 1.14 Schematic of FIB mechanisms. In the case of etching, focused ions bombard the surface of the sample, sputtering off sample in a process known as milling. In some instances, an etchant gas is used to aid in the removal. For deposition, a precursor of a metal compound is injected near the surface of the specimen, where the ions interact with the metal species and adsorb onto the sample; the remainder of the compound is pulled into the vacuum.

1.7 Electron Beam-Induced Current (EBIC)

Electron beam-induced current (EBIC) is a powerful semiconductor analysis technique where the electronic activity of a specimen can be studied with high spatial resolution. Particular areas of a sample with high current density can be detected. Due to the fact that simultaneous EBIC and SEM micrographs can be obtained, a correlation between the two can be made, thus the location of p-n junctions and specimen defects in relation to structure can be determined (Figure 1.15). Commonly used as a failure analysis technique, EBIC is, however, utilized as a means to locate where the peak EHP generation and collection takes place.

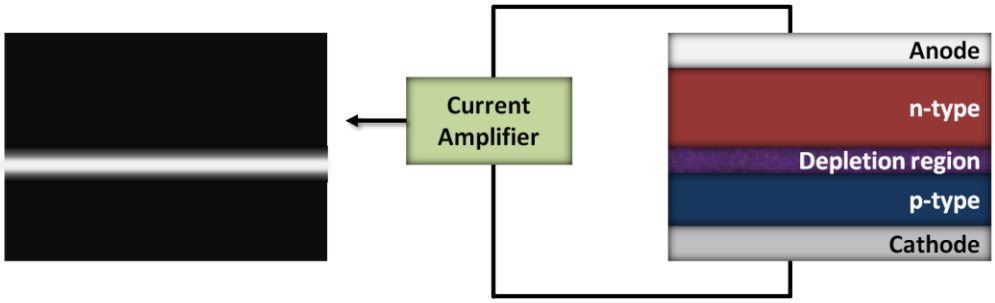

Figure 1.15 A generic illustration of EBIC of a semiconductor where the electron beam is normal to the page. As a high energy electron beam rasters over the sample, EHPs are being generated; however, only at the p-n junction are those electrons and holes able to be extracted.

EBIC measures the current generated from a sample and amplifies it to produce a grayscale image where the contrast is between that of positive current extraction versus a lack thereof. As aforementioned in Section 1.2, for a bulk semiconductor, there is a p side (predominantly positive charges) and an n side (majority of negative charges) where in the middle lies a p-n junction. As a high energy electron beam strikes the depletion region, an electron-hole pair is generated. Each charge then moves into the opposing direction (electrons move toward p side, and vice versa), where those charges are then referred to as minority carriers. These are then swept to their respective electrodes (minority carrier diffusion), similar in the case of how the photovoltaic functions; however rather than reaching an external load, the current passes through a current amplifier which then sends a signal to a Gatan DigiScan and then finally to a computer thus producing a grayscale image. EBIC contrast exists based on this premise that there are fluctuations in recombination, such as at defects, i.e. dislocations in single crystalline PVs, where there is low charge collection, while p-n junctions are the

opposite.[59] One important distinction is that the resolution of EBIC is more so limited by the generation volume as opposed to the minority carrier diffusion length.[59,60]

Under short circuit current conditions, the collected current is given as

$$I_{CC} = \frac{I_b E(1-f)}{E_{eh}} \sum \frac{\Delta w}{w} = I_G \sum \quad (1.2)$$

where I_b is the SEM electron beam current; E, electron beam energy; f, energy fraction of incident electron beam that is reflected from the sample surface; E_{eh}, carrier pair creation energy; Σ, charge collection efficiency; $\frac{\Delta w}{w}$, fraction of total depletion width over which carriers drift; and I_G, maximum beam generated current.[61] Equation 1.2 allows one to approximate the current able to be collected under the simplest conditions at a p-n junction. Additionally, diffusion lengths and recombination velocities can also be determined.

Similar to the absorption of the light where only wavelengths at or below the band gap are absorbed, EHPs are generated by an electron beam 3 times the material band gap.[62] At a 1 nA beam current operating at 5 kV, there are approximately 6 x 10^9 EHPs being generated at any given second. Any excess energy is converted to heat, while the remainder is contained in a combination of backscattered, secondary, and Auger electrons as well as X-rays.[59]

CHAPTER II

EXPERIMENTAL METHODS

2.1 Chemicals & Supplies

Chemicals were purchased and used without further purification: *N*-tri-octyl-phosphine oxide (Sigma, 90 %), cadmium oxide (Strem Chemicals, 99.99 %), selenium powder (Strem Chemicals, 99.99 %), tri-n-butylphosphine (Sigma, 97 %), anhydrous toluene (Sigma, 99.8 %), ethanol (180 proof), hexanes (Sigma, 99.99 % trace metals basis), anhydrous pyridine (Sigma, 99.8 %), and anhydrous 1,2,4-trichlorobenzene (Sigma, >99 %), poly(3-hexylthiophene-2,5-diyl) (Rieke, regioregular product 4002-E). Dodecylphosphonic acid was synthesized in the laboratory.

Indium tin oxide (ITO) glass slides (Delta Technologies (CG-61N-0115, 25 x 25 x 1.1 mm polished float glass), sheet resistance of 15-25 Ω), Triton X-100 (Sigma), poly(ethylenedioxythiophene):poly(styrenesulfonate) (Sigma), d-sorbitol (Sigma, >98 %), 1-methyl-2-pyrrolidinone (Sigma, 99+ %, ACS Reagent).

2.2 Synthesis of CdSe Nanorods

CdSe nanorods were colloidally synthesized by a modified procedure from Xi and Lam.[63] The synthetic setup is shown in Figure 2.1. In a 25-mL round bottom flask, 1.25 g (3.23 mmol) of TOPO, 0.500 g (2.00 mmol) of DDPA, and 0.128 g (0.997 mmol) of CdO were heated and stirred to 200 °C while purging under Ar. The brown colloid was then

further heated to 330 °C until the solution became clear. The temperature was reduced to 310 °C at which a clear solution of TBP (0.60 g, 3.0 mmol) and Se (0.08 g, 1.0 mmol) was injected at two minute intervals in four portions. Color change occurred approximately 15 seconds after the initial injection. For 30 minutes at 310 °C, the nanocrystals were grown. Compressed air was utilized to cool the flask to 90 °C, after which the solution was transferred to a pre-weighed 11-dram glass vial fitted with a Teflon cap. Toluene and ethanol (approximately 1:4) were added to the vial, and then centrifuged at 2500 rpm for 10 minutes.

Figure 2.1 Nanocrystal synthesis setup.

A total of four toluene/ethanol washes were done in inert atmosphere; the clear supernatant was discarded and the pellet of nanocrystals was dried after each cycle. After the last cleaning step, the pellet was dispersed into three mL of pyridine. This solution was stirred and heated at 115-120 °C for 1.5 hours before being flocculated by an excess of hexanes (1:5). The vial was centrifuged at 2500 rpm for 10 minutes. This pyridine exchange process was repeated two additional times. The calculated mass of the vacuum-dried nanocrystals was finally dispersed in a 1:9 ratio of pyridine and TCB; a 30 mg/mL solution was prepared for device fabrication.

2.3 Device Fabrication

ITO glass slides were cleaned by ultrasonication in Triton X-100 (3 % by volume), acetone, and isopropyl alcohol for 10 minutes each. Each slide was subsequently dried under a stream of nitrogen and stored in a 110 °C oven for three hours or more to ensure complete drying.

A PEDOT:PSS solution was prepared via a method by Jönsson.[64] In a glass vial fitted with a Teflon cap, 2.5 g of PEDOT:PSS was mixed with 2.5 g isopropyl alcohol and stirred at room temperature. NMP (0.128 g) along with 0.071 g d-sorbitol were directly added into the vial; the solution was stirred again at room temperature for 15 minutes. The final mixture was stored at 4 °C until further use.

Prior to the active layer, the electron-blocking PEDOT:PSS layer was deposited in ambient air. The PEDOT:PSS solution was warmed to about 70 °C, gently venting by unscrewing the cap as necessary. Meanwhile, the ITO slides were removed from the

oven to cool to room temperature. Each ITO slide was coated with the PEDOT solution and spun at 1500 rpm for one minute on a spin-coater. A layer of PEDOT is evident when the slide appears to have a rainbow tint to it. The slides were then transferred to a 120 °C hot plate to anneal the PEDOT; the annealing process was 20 minutes. Until device fabrication, these prepared slides were stored in a 110 °C oven in air.

Under inert atmosphere (Angstrom glovebox), the following processes were conducted. Solutions of P3HT at 30 mg/mL in TCB were mixed at a 1:9 wt % with the aforementioned dispersion of CdSe NRs (see section 2.2); this blend was then coated (with a uniform, well-covered layer of solution) and spun onto a PEDOT:PSS/ITO glass slide at 500 rpm. Depending upon the desired thickness of the layer, this step may be repeated up to two additional times. The photoactive layer was annealed under vacuum for 15-20 minutes at 120 °C. Lastly, 100-250 nm thick aluminum contacts were resistively deposited via an Angstrom Åmod system.

There are tricks to depositing Al onto the CdSe:P3HT layer. The parameters can change each time it is used; however, the settings described here can provide a good starting point. First, two 99.99 % pure Al pellets from the Kurt J. Lesker Company were loaded onto a single-use tungsten boat (the type of boat is important as it will affect how much power to apply). By using two pellets, this will allow for approximately 100 – 120 nm worth of Al. If thicker contacts are desired, venting the chamber to exchange the boat and adding more pellets will be necessary; another option is to use two “stations” for Al deposition.

In the software, input the intended thickness with the rate value below 10 Å/second (ideal is 2 Å/sec). The ramp and soak maximum power should be approximately 10 % lower than the deposition parameter. In this case, 26 % was used. "Ramp2" time was set at 60 seconds, while the "Soak2" was 120 seconds. "Ramp1" and "Soak1" were set at zero. The shutter delay was also omitted as it quickly drains source material. PID settings are the most variable components, as it can affect the deposit significantly. The P, set to 155; I, set to 6; and D, set to 0. The maximum power, as alluded to earlier, was 35 %.

2.4 Device Characterization (Testing)

Devices were tested for their efficiencies via a solar simulator; one sun intensity was generated by a ScienceTech SF150B AM1.5G. This system was calibrated with a NREL Si standard to one sun intensity (via distance). A LabView program was written to calculate the efficiency, open circuit voltage, short circuit current, fill factor, among other factors. Means of calculating the efficiency and other parameters can also be done with Excel, as shown in the Appendix.

2.5 Sample Preparation

2.5.1 TEM – Nanocrystals

Sample preparation of nanocrystals for TEM analysis is straightforward. From a stock of solution of nanocrystals, a single droplet is transferred to a separate vial. With the same solvent, the droplet is diluted until just optically transparent. A single droplet

aliquot from the dilute solution is dropped onto the TEM grid (Ted Pella, 1822-F) held by anti-capillary tweezers and allowed to dry for approximately one minute. A flat edge of a Kimwipe is used to wick away excess solvent from the drop-cast.

The TEM grid that may come with a Formvar polymer during processing may be removed by solvent rinses. Using anti-capillary tweezers, the grid is sequentially dipped into acetone, chloroform, and finally acetone again. The grid is allowed to dry on the tweezers, and then the above sample preparation method is commenced.

2.5.2 TEM/STEM – Devices via Tescan Lyra3

Complete device characterization using TEM was prepared by a dual beam FIB/SEM (Tescan Lyra3 at Middle Tennessee State University). The device was cleaved via diamond scribe and Fletcher "Gold Tip" nipping pliers as to isolate one or several Al contacts; this was then mounted onto an appropriate pin stub with copper tape making sure to contact the ITO. Also loaded into the SEM chamber is a FIB lift-out grid (Omniprobe copper lift-out grid, Ted Pella product #460-204), where the grid is sandwiched onto a grid holder (PELCO small FIB grid holder, Ted Pella product #15464), as seen in Figure 2.2.

The ion beam on the Lyra3 is 55° offset from the pole piece; therefore the stage must be tilted 55° to mill or deposit onto the specimen at plan view with a working distance of 9 mm. First, a Pt protection layer was deposited on the region of interest (ROI) (on the area of the specimen that will be lifted out, known as a lamella). The area around the protected region was then staircase-milled (Figure 2.3) at the front and back

of the ROI where the length, width, and depth are proportional to the depth at which the lamella will be exposed – the length should show the bottom edge of the lamella when viewed from the SEM.

Figure 2.2 The FIB lift-out grid (left) and the holder for the lift-out grid (right) for use with the Tescan Lyra3. Images from Ted Pella.

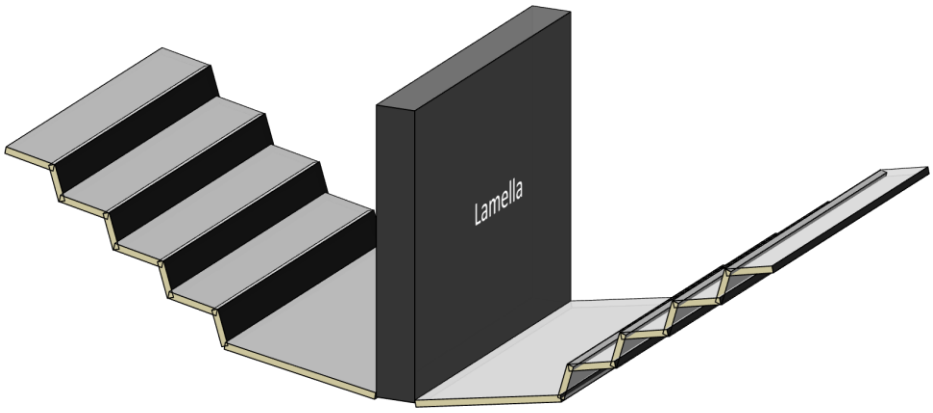

Figure 2.3 Staircase mill for preparation of lamella in the Lyra3.

The stage was then tilted back to 0° for the next steps. First, the stage was rotated to the lift-out grid; alignments were made so that the grid would be ready for the lamella. Most importantly, the position was saved afterwards. The stage was

rotated back to the sample: the left edge and bottom of the sample were milled in parallel to partially release the lamella. The right side was preserved to anchor the sample. Once cut, the nanomanipulator was introduced. The tip of the manipulator was brought as close to the left side of the lamella as possible. The x and y directions were judged by the SEM, while the FIB imaging assisted in the z-axis determination. With the nanomanipulator situated by the lamella, the GIS needle was inserted and Pt was used to weld the tip of the manipulator onto the left side of the lamella. When the specimen becomes securely attached, the right side of the lamella was milled to completely release it.

With the lamella attached to the nanomanipulator, the stage was lowered and rotated so that one of the posts on the lift-out grid was in place to "receive" the sample. The lamella was situated at the post and, once again, Pt was used to weld the right side of the specimen. When it is attached to the post, the Pt connecting the nanomanipulator and sample was milled off; the manipulator was then retracted. At this time, the stage was returned to a 55° angle. The lamella was polished with sequentially lower kV ion voltages to an optimal TEM specimen thickness; this can be judged by the transparency of the lamella under the electron beam in SE mode.

2.5.3 TEM/STEM – Devices via Zeiss Auriga

Complete device characterization using TEM could also by prepared by the dual beam FIB/SEM at the University of Tennessee Knoxville with their Zeiss Auriga. As with Section 2.5.2, the device was cleaved as to isolate one or several Al contacts; this was

then mounted onto an appropriate pin stub with carbon and copper tape making sure to contact the ITO for grounding. Also loaded into the SEM chamber is a FIB lift-out grid (Omniprobe copper lift-out grid, Ted Pella product #460-204 or Pelco copper lift-out grid, Ted Pella product #10GC04), where the grid is sandwiched onto the grid holder with up to two sampled on either side (as shown in Figure 2.3).

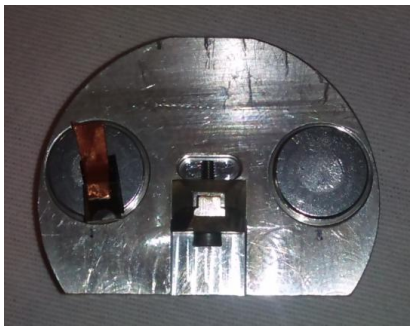

Figure 2.4 The "TEM" holder for FIB lift-outs on the Zeiss Auriga. To the left and right are sample holders, while the center is reserved for a lift-out grid (sandwiched between two metal plates).

The ion beam on the Auriga is 54° offset from the pole piece; therefore the stage must be tilted 54° to mill or deposit onto the specimen at plan view, with a working distance of 5 mm (coincidence point). First, a Pt protection layer was deposited on the ROI at a probe current of 20 – 50 pA running at 30 kV (ion beam). The area around the protected region was then trapezoidally milled at the front, back, and left sides (30 kV, 2 nA) of the ROI where the length, width, and depth (see Figure 2.5) are proportional to the depth at which the lamella will be exposed – the length should show the bottom edge of the lamella when viewed from the SEM.

The thick lamella was then thinned to an approximate 200 – 300 nm thickness. Probe currents starting at around 200 pA were used to begin with, then they were sequentially lowered, i.e. 100 pA, 50 pA, 20 pA. The thinned region was measured using the distance measurement feature in FIB mode.

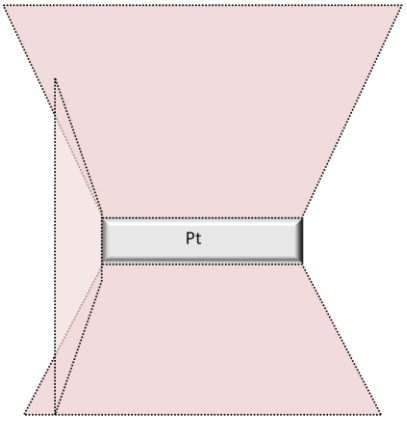

Figure 2.5 Trapezoidal trench milling schematic for lamella preparation.

The stage was then tilted back to 0° for the next steps. The bottom and left edge of the sample were milled sequentially to partially release the lamella (30 kV, 2 nA); the right side was not cut to anchor the sample. Evidence of the release of the bottom edge can be determined by either tilting the sample (to view in SE mode) or ensuring the depth of the cut is deep enough so that a section of the front trench is etched. Once the cuts have been made, the Kleindeik needle was inserted. The needle was then brought close to the lamella, using both the SEM and FIB (30 kV, 20 pA for the latter) scanning modes at the fastest scan rates to judge the distance between the sample and needle

tip. As mentioned in the prior section, the SE mode is primarily used to approximate the x- and y-directions, while the FIB is used for the z-direction. When the tip almost touches (or touches) the top left corner of the Pt protection layer, a weld of Pt from the Kleindeik to the lamella was made. The remaining right bridge holding the lamella to the bulk sample was milled as well; the lamella should be free from the bulk.

With the lamella attached to the needle, the stage was rotated so that one of the posts on the lift-out grid was in place to "receive" the sample. The lamella was situated at the post and, once again, Pt was used to weld the specimen. When it is attached to the post, the Pt connecting the nanomanipulator and sample was milled off; the manipulator was then retracted. At this time, the stage was returned to a 54° (or 56° / 52°) angle for the finishing polishing steps (performing the coincidence and eucentric alignments again). The lamella was polished with sequentially lower probe currents to an optimal TEM specimen thickness. "Windows" were made to achieve various electron transparencies.

2.5.4 SEM EBIC

Specimen preparation for EBIC analysis is similar to that of a thin film device methodology. The tools used for the following are shown in Figure 2.6, where an emphasis is placed on C (Gatan Ilion+ Ar ion polisher).

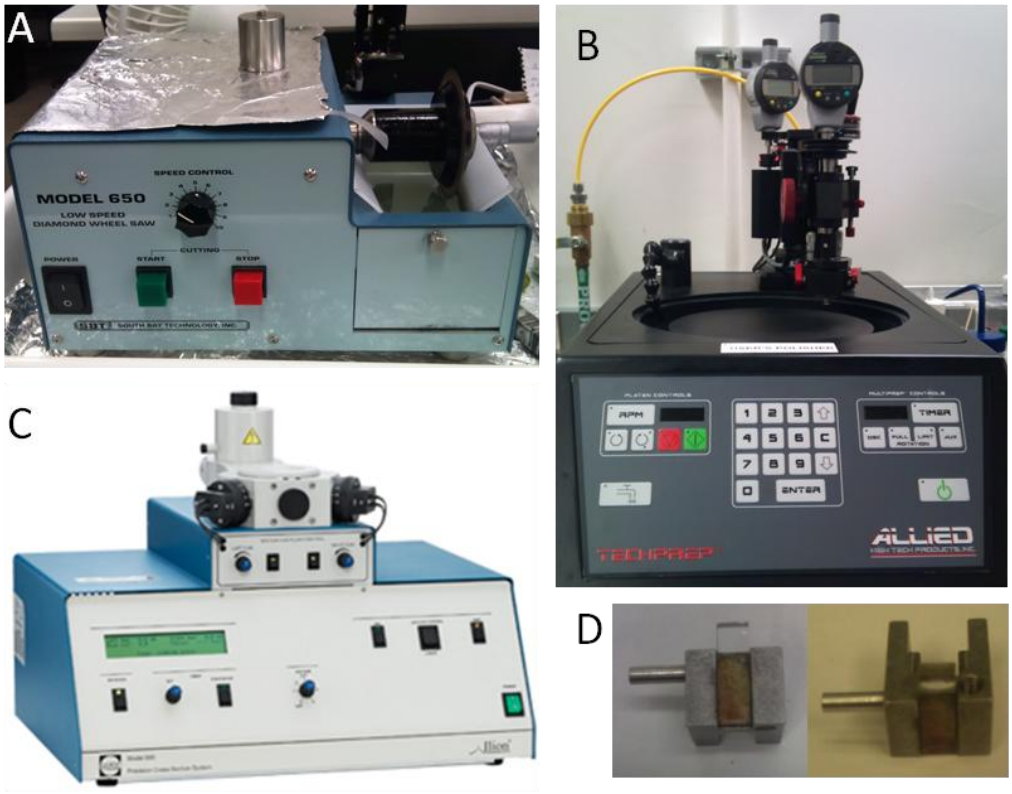

Figure 2.6 SEM EBIC sample preparation tools. (A) Low speed diamond saw, (B) polishing wheel, (C) Ilion+ Ar ion polisher, (D) polishing wheel sample holder/stubs.

2.5.4.1 CdSe:P3HT

As a note: this device is solvent sensitive, so no solvents can be used for the sample preparation. First, the device was cleaved by using a diamond tip scribe to isolate a single Al contact. Further diamond saw cutting (South Bay Technology, Inc., Model 650, without oil lubrication) would expose a cross-section of the contact for the next steps. The sample was attached to a microscope slide by a resin/wax with the sample facing the blade.

In order to fine polish the cross-section, the sample was mounted onto a holder (see Figure 2.6D) with wax. Utilizing a polishing wheel (Allied High Tech Products, Inc., TechPrep), a dry fine polish was performed. Starting with a larger (i.e. 30 μm) grit lapping paper to coarse smoothen the cross-section, the polish was done at 10 – 25 rpm with the sample facing toward the rotation of the wheel. Next, this was followed by continuously finer grit paper (i.e. 9 μm, 6 μm, 3 μm) to further polish the specimen. The sample was then removed from the stub (with heat and then acetone) and transferred onto a Gatan Ilion+ blade for Ar ion milling. The polishing wheel step can be omitted if the cross-section of the pad appears to be "clean," i.e. no nicks, overhang of loose metal, etc., under an optical microscope.

2.5.4.2 PbS depleted-heterojunction

The device was mounted onto a microscope slide using wax, with the device facing the glass. The diamond saw (Figure 2.6A) was used to both isolate and make the initial cross-section cut on the pad (Figure 2.7) – Isomet oil was used to lubricate the blade. Once cut, heat (150°C) released the sample from the glass slide, and then acetone and methanol soaks were used to clean the samples of the wax. The section of interest was mounted onto the Ilion blade and then further polished.

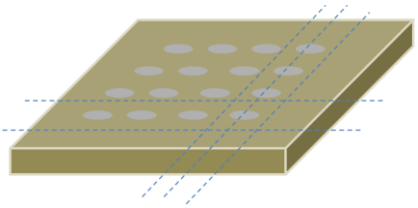

Figure 2.7 PbS device schematic where the dashed lines indicate where the diamond saw would cut.

2.5.4.3 Final polish and sample mounting

Once the isolated pad has been roughly polished (see sections 2.5.4.1 or 2.5.4.2), Ar ion polishing of the cross-section face is done (Gatan Precision Cross Section System Ilion+, Model 693, Figure 2.6C). Minimal amounts of Loctite super glue from a paper point was used to mount the sample onto the milling blade, where a 50 µm excess remained over the edge of the blade. At 5 kV for one hour at liquid nitrogen temperature, the sample was ion milled for the final polishing step. Milling is evident by a slight parabolic feature on the sample – this is where the imaging will take place.

In order to provide a larger area of contact for the EBIC probe, In wire was pressed onto a thoroughly cleaned area of the TCO. The probes of the EBIC stage were contacted to the In and the back contact.

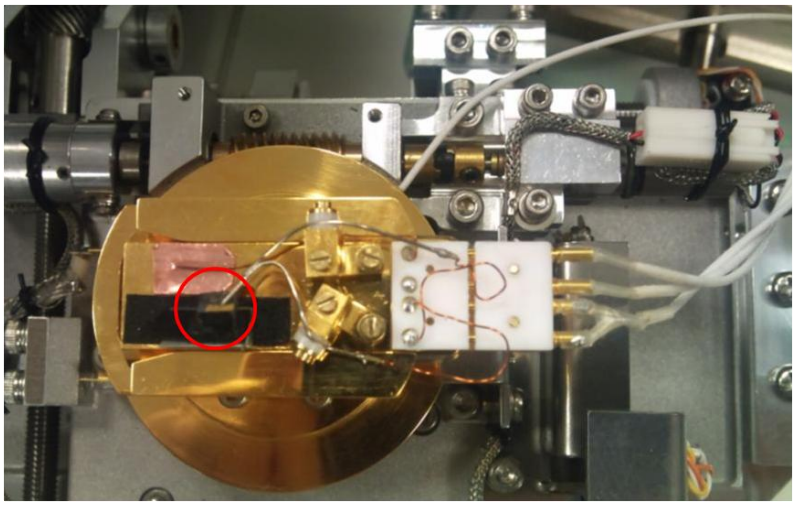

Figure 2.8 The SEM EBIC stage. The sample is circled and the probes each touching the anode and cathode, repectively.

The prepared specimen was then mounted with carbon tape onto the modified (addition of a 45° wedge to allow for 90° sample analysis) EBIC stage, as shown in Figure 2.8, where the sample is circled in red. The polished cross-section was aligned toward the edge of the wedge. Two probes on the stage are each contacted to a cathode or anode; the probes are connected to throughputs which extend externally from the chamber to a current amplifier. The SEM door was removed to change the stage to the EBIC accompanied one and I-V curves were taken to ensure proper connections were being made throughout the process. Once replaced, the chamber was allowed to evacuate for 1.5 hours before further use, or until the designated 6 x 10^{-4} Pa was reached.

2.6 SEM EBIC Measurements

For the best imaging, the stage was tilted to a 45° angle and the z-axis was brought to the smallest working distance possible without touching anything in the chamber/polepiece (approximately 12 mm). The imaging parameters necessary for SEM EBIC are primarily sample-dependent, which includes factors such as accelerating voltage, probe current, and image acquisition gain/sensitivity. Typical parameters for nanocrystal-based devices: 5 kV accelerating voltage, high probe current, and 5 x 10^7 gain. This is a good baseline to start imaging and can be adjusted as necessary. More specific details can be found in the respective chapters of each device.

CHAPTER III

DIRECT ELECTRONIC PROPERTY IMAGING OF A CDSE:P3HT PHOTOVOLTAIC DEVICE BY ELECTRON BEAM-INDUCED CURRENT VIA SCANNING ELECTRON MICROSCOPY

3.1 Introduction

Nanocrystal-based third generation photovoltaics have developed steadily over the past few decades with a recent achievement of 8.5% power conversion efficiency.[36,65,66] However, this significant accomplishment in nanocrystal photovoltaics is still unmatched to the devices' theoretical efficiency of ~60%, nor is it close even to commercialized semiconductor film-based solar cell technologies.[6] The hybrid bulk heterojunction (BHJ) device architecture, which is studied here, consists of doped nanocrystals (CdSe nanorods) dispersed in an opposing polarity medium (in this case, P3HT polymer), in which space charge regions are located at the nanocrystal-polymer interface. The highest efficiency nanocrystal device fabricated to date uses a Schottky-like configuration better known as a depleted-heterojunction showing 8.5% efficiency,[36] while the device architecture of interest in this study has a lower record efficiency of 2.6%.[28]

An understanding of why the nanocrystal-based hybrid BHJ device fails to compare with other photovoltaics is critical to further progress solar cell technologies. It is widely accepted that the primary limiting factor of nanocrystal-based solar cells is the high density of surfaces within the device volume creating several surface state

carrier recombination centers. Passivating these surface state centers is known to improve the device performance including carrier mobilities and open circuit voltage, Voc.[6,30,65] However, for nanocrystal-based devices, maintenance of electron conducting pathways throughout the absorber layer is crucial for high efficiency. It also stands to reason that an increase in the percolation pathway lessens the ability for the free charge carriers to be extracted to their respective electrodes due to higher possibilities of carrier recombination during the migration, thus a decrease in the overall efficiency would occur.[67] Prior studies of the architecture of interest have been conducted utilizing different techniques. One example is the application of time-resolved microwave conductivity to directly probe the charge generation and decay times in the active layer.[68] Similarly, Albero et al. performed experiments utilizing time-correlating single photon counting and photo-induced transient absorption spectroscopy to investigate exciton formation, carrier separation, and carrier recombination;[69] Noone et al. also used the same technique for their studies.[70] In the former case, it was demonstrated that the presence of nanocrystals influenced the charge carrier recombination rate, while in the latter, it was found that polaron lifetimes were increased with the addition of an inorganic component such as CdSe into a polymer system.[69,70] Although these types of studies are significant in regards to the CdSe:P3HT charge carrier lifetimes, they lack a spatial characterization. Electron beam-induced current (EBIC), on the other hand, is a powerful semiconductor analysis technique that has long been used toward studying integrated circuits,[71] transistors,[72] nanowires,[73] solution processed organic solar cells,[74] and thin film photovoltaics that provides direct

imaging of the specimen.[7,61,75–78] Despite the numerous prior applications of EBIC, it has not yet been used toward characterization of photoactive nanocrystal-based BHJs.

A direct map of percolation pathways is obtained with electron beam-induced current (EBIC) at a resolution of about 100 nm. It is shown that only a very thin layer of the nanocrystals adjacent to the cathode side are efficient at carrier generation in the device. These results emphasize the importance of finding a means to link the nanocrystals so as to produce an interconnected network for the electrons to traverse within the device.

The SEM-EBIC measurements have been complemented with scanning transmission electron microscope (STEM) techniques in order to correlate the structure and nanocrystal dispersion to the electronic properties of these devices. By appropriately coordinating these data, critical information regarding the device deficiency has been elucidated. The results of these measurements show the first steps toward necessary improvements that need to be made to these devices.

3.2 Methods & Results

The solar cell used for this experiment is a hybrid bulk heterojunction architecture consisting of inorganic (electron accepting CdSe nanorods) and organic (electron donor poly-3(hexylthiophene) or P3HT polymer) components (synthesis of the nanorods and fabrication of the device can be found in Sections 2.2 and 2.3, respectively).[27] Although it is utilized as a simple standard for BHJ nanocrystal-based photovoltaics, many aspects that have inhibited its efficiency have not yet been well

characterized in a post-fabricated state. A schematic of the EBIC experiment on this device is shown in Figure 3.1.

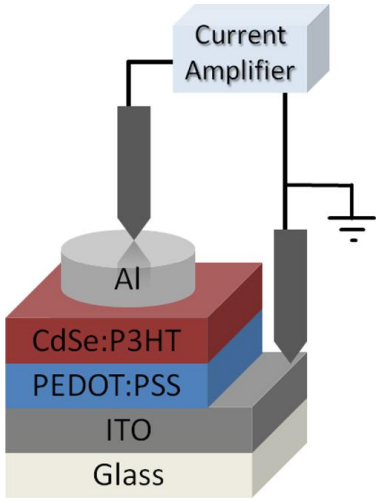

Figure 3.1 Schematic of the EBIC connections.

Due to the sensitivity of EBIC to surface recombination and topography, very careful sample preparatory techniques were followed. To prepare the samples for EBIC, each specimen was diamond saw cut and polished with a 1 µm diamond polishing cloth to reveal the cross-section of the device. Argon ion milling (Gatan Model 693, Ilion+) at liquid nitrogen temperatures was used to mitigate the surface damage caused by the polishing. After milling, the sample was mounted onto an EBIC stage, which was inserted into a Hitachi S4800 FEG-SEM equipped with a Gatan SmartEBIC system. Samples were analyzed at an accelerating voltage of 5 kV and a gain of 1×10^8.

Cross-sectional SEM EBIC measurements have been performed to understand the carrier separation properties of the active layer that limit the device efficiency

(Figure 3.2). The contrast in the EBIC image shown in Figure 3.2 is the EBIC current divided by the probe current, ranging from the beam current (~400 pA) to ~4x the beam current. The majority of extracted carriers are those that are generated in the CdSe:P3HT layer close to the Al interface. These results show that only the carriers generated within a few nanometers of the CdSe:P3HT close to the Al contact are capable of both separating and traveling to their appropriate contacts without recombining. This thin region seems to be the only photoactive part of the device. The remainder of the CdSe:P3HT layer, however, is mostly dark indicating a significant presence of carrier recombination before collection.

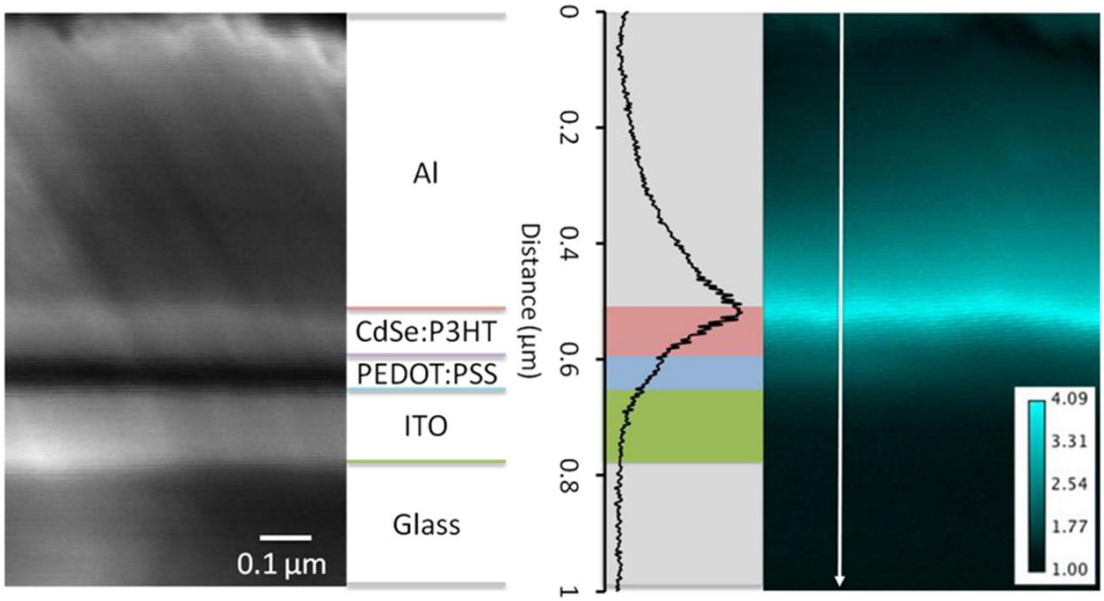

Figure 3.2 SEM (left) and EBIC (right) scans with the layers identified corresponding to the line profile. The line profile was taken where indicated by the white line on the EBIC map. Current output scale is in nA.

Given that each incident electron will produce ~775 – 1,050 carriers for a 5 kV accelerating voltage, the EBIC efficiency can be calculated. Assuming a 100% efficient device will produce an EBIC current that is ~775 – 1,050 times the beam current, which was calculated from Eq. 3 in Yacobi et al.,[79] the maximum current recorded (4x the beam current) for these samples in the active region would indicate a maximum efficiency of only 0.4 – 0.5 % if all of the carriers were absorbed in the active region. This is not the case, because only a small percentage of the absorbed electrons interact with the very thin active region and surface recombination on the cross-sectional face, which would not occur in a bulk device, decreases the collection efficiency. Therefore, the efficiency of the active region cannot be calculated accurately. However, it is expected that the actual efficiency of the active layer is much higher than the calculated value.

Current-voltage measurements have shown the Al to be the electron contact and the TCO the hole contact. The band structure of the device bolsters the argument that electrons have a preferable route to move from the conduction band of the CdSe to the Al.[30] The holes on the other hand, would ideally be forced into the conductive polymer where it would either exit at the anode or recombine with a free electron.

The asymmetry of the collected current profile across the Al and CdSe:P3HT layers is due to the electron excitation volume dependence on the target material. Electron flight path simulations (Casino) for each target material have been conducted to clarify this asymmetry (Figure 3.3).[80] As the electron beam rasters over the

CdSe:P3HT layer and into the Al layer, the excitation volume increases; therefore, the beam interacts with the active region at farther distances when the beam targets the Al layer compared to the CdSe:P3HT layer.

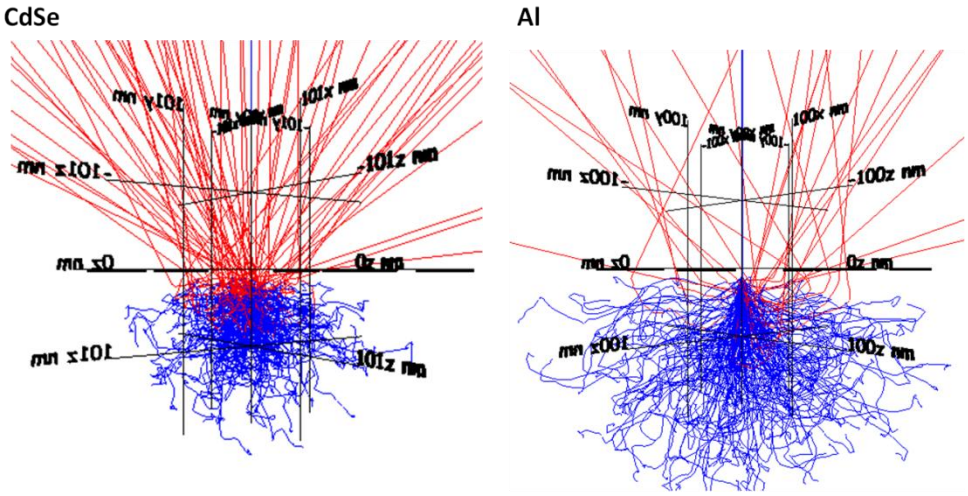

Figure 3.3 Monte Carlo simulations of 5 kV electron beam interaction with CdSe and Al; the latter shows a high interaction volume which addresses some of the confusion with why EBIC signal was coming from the Al region in Figure 3.2.

Localization of the EBIC to a thin layer of the CdSe:P3HT close to the Al contact can be explained by the proximity of the nanocrystal to the cathode where the electrons are extracted. Free electrons that are directed into non-Al interfacing nanorods are unlikely to flow to the electron-collecting contact without recombining. Therefore, electrons are highly immobile when translating between nanorods. On the other hand, the EBIC results suggest that holes are much more mobile than the electrons as they are able to traverse to the TCO layer through the entire CdSe:P3HT layer without significant

recombination. This also suggests that the interfaces between Al/CdSe, CdSe/P3HT, and P3HT:PEDOT/ITO are well formed.

3.3 Conclusions & Outlook

The connection between each nanocrystal is, therefore, clearly one of the core limiting factors in the charge transport for CdSe:P3HT bulk heterojunction devices. As the pyridine ligands dissociate off the nanocrystal surface during the annealing process, there will be at least a 5 Å space between each nanorod; this is assuming that there are no TOPO or phosphonic acid ligands remaining, which would not only create a greater distance between the nanorods but also contribute to increased insulation of the charges. This is consistent with the results of Greenham et al. where their conclusion states that residual lengthy ligands on the surface of the nanorod inhibit the charge transport from nanocrystal to nanocrystal.[81] Subsequently, it would be difficult for the electron to percolate from one rod to another. The lack of interaction between the nanocrystals as well as the internal electric field at the nanocrystal/P3HT interface confines the electron to the nanorod for a time frame that results in recombination. Additionally, as demonstrated in Figure 3.4, distribution of the nanorods can be uneven, where regions of aggregates and voids form. Based upon current results, a means to connect the nanorods, creating a continuous network would be necessary to allow the electron transport to be undisturbed. Both SEM EBIC and STEM imaging data sets support these conclusions.

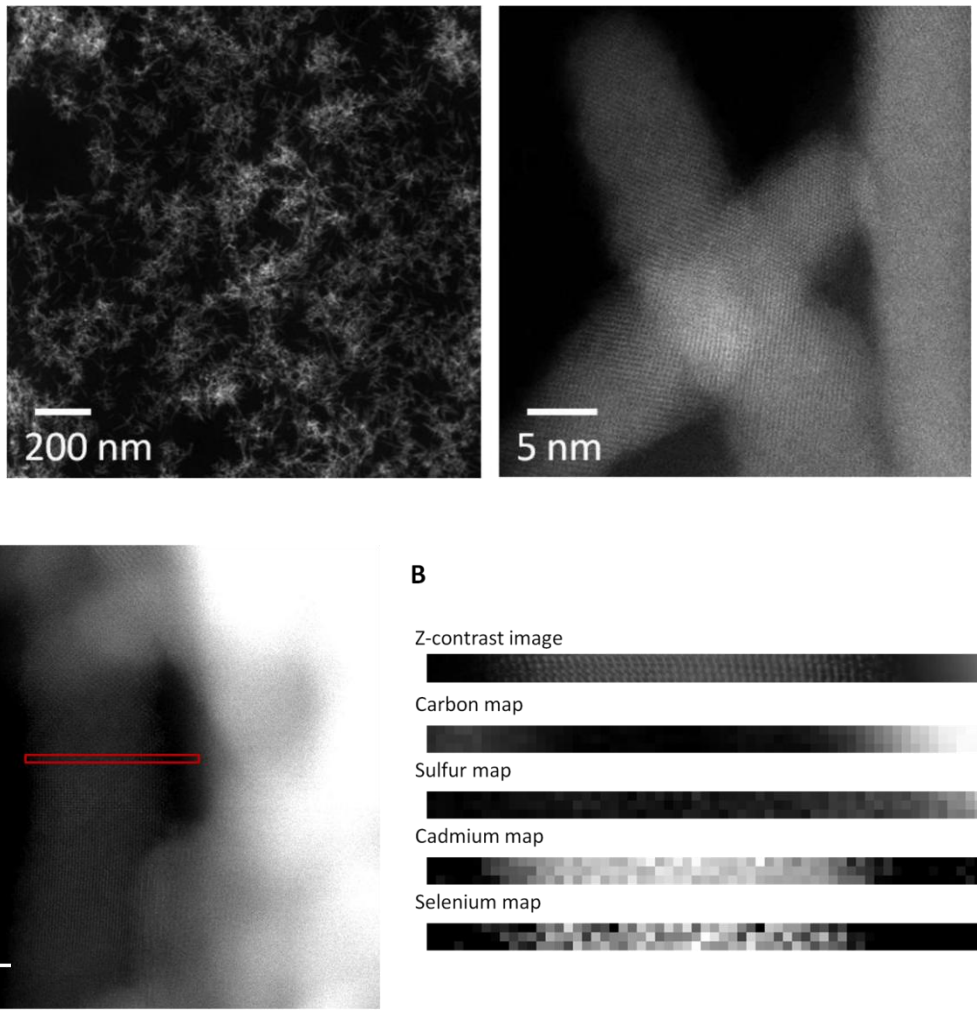

Figure 3.4 STEM micrographs of CdSe nanorods dispersed in P3HT polymer. (A) and (B), which are maps of the highlighted region in (A), show electron energy loss spectroscopic data indicating the presence of P3HT surrounding the rods.

As shown, significant information can be elucidated from SEM EBIC studies; however, without having a higher resolution microscope, the interfacial and potential nanocrystal defect studies for this type of device is impossible since SEM cannot resolve individual nanorods at the current size regime. The next step to resolve this problem would be to apply EBIC towards an aberration-corrected STEM at a low accelerating

voltage. The challenge, ultimately, arises in the sample preparatory stages of the experiment. Once developed, the data able to be extracted from the experiment would provide indispensible information that the SEM EBIC method could not, such as direct imaging of nanocrystal-to-nanocrystal behavior and a more accurate depiction of where the charges tend to localize. When a better understanding of nanocrystal-based devices is found, improvements in the technology can be made and the next generation of photovoltaics can progress steadily.

CHAPTER IV

CORRELATION OF SEM EBIC AND HIGH-RESOLUTION EDS ANALYSIS OF A PBS QUANTUM DOT DEPLETED-HETEROJUNCTION PHOTOVOLTAIC DEVICE

4.1 Introduction

For years, the efficiencies of quantum dot (QD)-based solar cells suffered from poor performance.[82,83] However, within the last five years, the field has made immense progress.[32] With the Sargent group's initial discovery and proliferation at the University of Toronto, there has been significant renewed hope in this third generation photovoltaic technology. As of 2014, one of the best performing QD-based solar cells is a PbS depleted-heterojunction device with an induced photon-to-current efficiency (IPCE) of 8.5%.[25,36]

However, despite the performance of this solar cell in comparison to prior devices, there is still much room for improvement in terms of efficiency – the theoretical value is an impressive 66%.[24] Although testing the overall efficiency of a device is beneficial to determining how well a device functions, the smaller, less visible, shortcomings are still unknown. Further, the complicated and at times uncharacterized electronic nature of solution processed oxides and QD thin films often renders the devices that utilize them rather difficult to model with traditional electrical engineering approaches. In terms of nanoscale characterization of the electronic properties to assist in the determination of these limitations, there are very few techniques able to

accomplish such a task. Utilized here, is a means to achieve a direct mapping and correlation of both electronic activity and elemental analysis with high precision.

Electron beam-induced current (EBIC) is a technique that allows one to visually evaluate the current generation of a photovoltaic device by utilizing a high-energy electron beam to mimic photons and study the electron-hole pair generation and collection in a semiconductor. EBIC is ideal for studying this generation-III photovoltaic due to its ability to map and visualize features down to the microscale.[11] More importantly, defects such as contributions to a decreased short circuit current can be visualized. Furthermore, a correlation of EBIC with high resolution energy dispersive spectroscopy (EDS) of cross-sectional devices provides a better representation of where the charge carrier generation and collection take place.

4.2 Experimental methods

This study mostly focuses on the addition of engineered shallow trap defects and variations within layer thicknesses for comparison to an idealized ("pristine") DHC-QD PV device. These experiments serves, (1) as a convincing proof of principle experiment which shows that EBIC is a method in which even miniscule changes can be detected with ease, and (2) to bring to light new empirical findings with respect to the effect of QD polydispersity and optimization of layer thicknesses as a function of theoretical depletion widths (x_d).

The synthesis of the PbS quantum dots and fabrication of the devices follow the work presented by Pattantyus-Abraham, et al.[32] Briefly, the QDs are synthesized by a

hot injection route with lead oxide, bis(trimethylsilyl)sulfide, and oleic acid as a surfactant molecule. By modifying synthetic parameters, monodisperse particles with diameters of ~3.5 nm (E_g≈1.3 eV, 955 nm) and ~6 nm (E_g≈0.9 eV, 1450 nm) are prepared.[84] Device fabrication utilized FTO-coated glass slides onto which a layer of TiO_2 paste (Dyesol) was spun cast, treated with a solution of $TiCl_4$, and then annealed. The synthesized PbS were spin-coated onto the TiO_2 electrodes in a layer-by-layer fashion, with each successive layer being treated with MPA and methanol through dip-coating. The pristine device comprised of 11 coats at approximately 9 nm/layer; the exact values are in Table 4.1.

Preparation of the devices for EBIC is modeled after the procedure in Poplawsky, et al.[85] A sample is low speed diamond saw cut to expose a cross-section of a metal pad. This edge is then Ar ion ($Ilion^+$) polished so that it is topographically featureless (Figure 4.1). The latter is extremely important as EBIC is a surface roughness-sensitive technique, where prominent features would give false results. The process is explained in more detail in Section 2.5.4.2. EBIC was performed on a Hitachi S4800 SEM equipped with a Gatan SmartEBIC system (Oak Ridge National Laboratory, CNMS facilities).

Standard focused ion beam lamella sample preparation was utilized for STEM EDS analysis. The steps are described in Section 2.5.3. A Zeiss Auriga FIB/SEM (University of Tennessee Knoxville, JIAM) was used for this, while EDS measurements were taken using a Tecnai Osiris TEM/STEM (Vanderbilt University, VINSE).

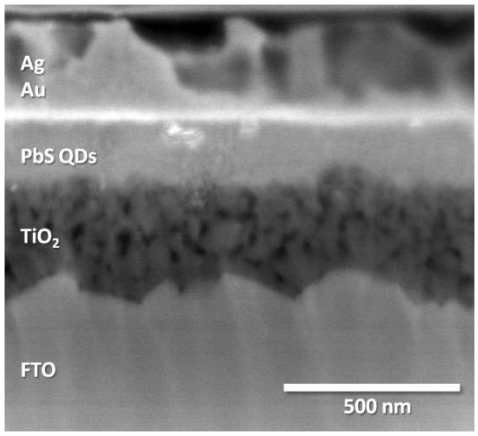

Figure 4.1 A cross-section of the PbS depleted-heterojunction device. Figure 1.6 shows a schematic of the device as well as a photograph of the fabricated device.

4.3 Results & discussion

Table 4.1 Average thicknesses of PbS and TiO_2 layers and measured device parameters.

Device	PbS avg thickness (nm)	TiO_2 avg thickness (nm)	η (%)	V_{OC} (V)	J_{SC} (mA/cm²)	FF	R_s (Ω)	R_{sh} (kΩ)
PbS 43	70	640	1.3	0.51	6.5	0.43	350.3	3.36
PbS 44	100	750	1.2	0.46	6.0	0.42	356.4	2.45
PbS 45	85	600	0.56	0.42	2.9	0.45	705.1	6.13
PbS 46	100	350	1.1	0.51	6.9	0.32	490.7	1.45
PbS 47	210	310	1.5	0.53	9.7	0.29	438.0	1.46
PbS 48	430	330	0.84	0.49	6.1	0.28	783.7	1.67

4.3.1 Overall analysis

The primary region of device activity occurs at the TiO_2 / PbS interface, with the generation extending farther into the TiO_2 layer for pristine devices, referred to in this

document as PbS 43 (Figure 4.2A). For both the thick TiO_2 (~600 nm, PbS 43) and thinner TiO_2 (~300 nm, PbS 46) with the same number of layers of QDs, the EBIC average line profiles appear to have a similar shape (Figure 4.2B). Note the decay of the line profile into the 600 nm thick TiO_2 for the pristine device extends a little farther into the TiO_2 than PbS 46, suggesting there is more electron hole pair (EHP) activity within that portion of the device. In order to investigate the origin of those signals, STEM EDS was employed (Figure 4.3). The STEM EDS maps of PbS 43 and 45 show that there is intermixing of the PbS QDs with the TiO_2 layer. At the porous regions of the titania, it can be seen that Pb and S signals are detected; this occurrence could be influencing the efficiencies of the devices, as it would provide a greater possibility for electron extraction with the increased surface area.

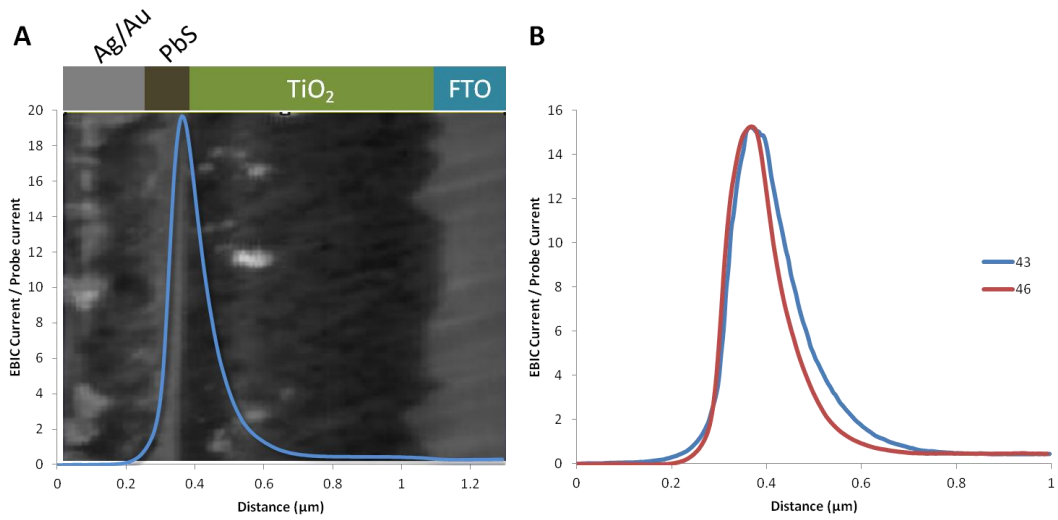

Figure 4.2 (A) An EBIC average line profile shown over the SEM of the region of interest. Signal peaks at the QD / TiO_2 interface. (B) Average line profiles of both PbS 43 (600 nm thick TiO_2) and 46 (300 nm thick TiO_2) showing consistent signal intensity.

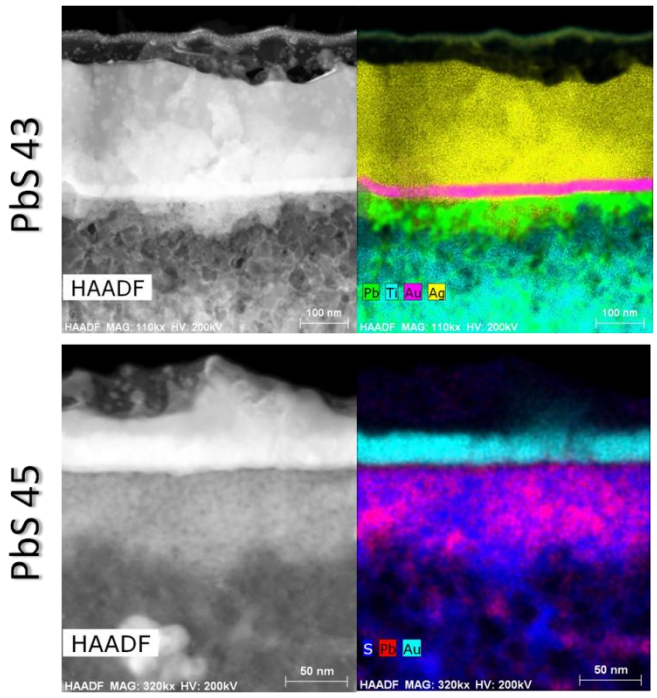

Figure 4.3 PbS 43 ("pristine") and PbS 45 (20% b.w. shallow trap defect) STEM EDS maps.

4.3.2 Defect engineering

As shallow potential well traps in the form of lower E_g QDs are introduced into the active layer the average line profile changes in the EBIC scans. With a pristine device (monodisperse 1.3 eV PbS particles), the peak onset begins near the Au / PbS interface, extending with maximum signal at the PbS / TiO_2 junction; a gradual decay into the TiO_2 is shown as well. In the case of non-pristine devices of 5% b.w. inclusion of 0.9 eV PbS QDs, very little of its effects could be detected by EBIC; moreover, the measured macroscale parameters (Table 4.1) were comparable, and again, minimal differences were observed. These devices, despite their sensitivity to nanoscale defects, can maintain high efficiencies at a small percentage of defects, as shown by EBIC.

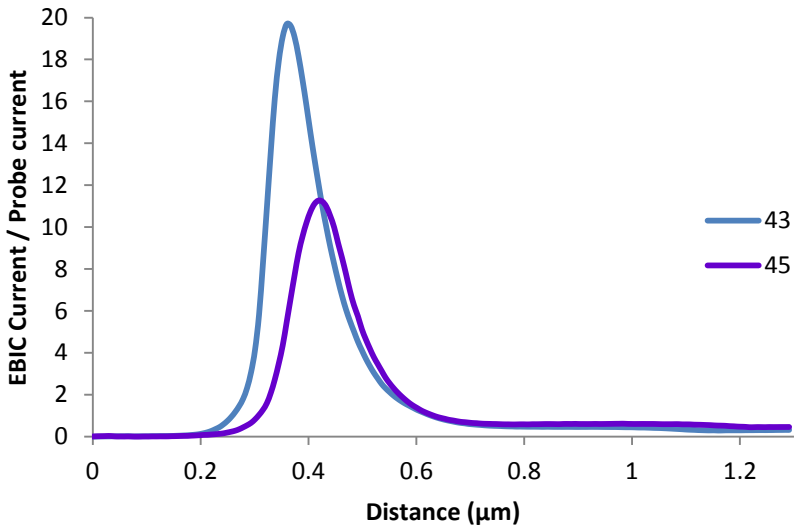

Figure 4.4 Average line profiles of the pristine PbS 43 and defected PbS 45. The intensity change corresponds to the drastic change in J_{SC} values measured. The location of the p-n junction remains at the PbS / TiO_2 interface, but the widths are different.

With 20% b.w. of larger nanocrystals, primary EHP generation occurs at a narrower region of the PbS layer compared to a pristine device (Figure 4.4). These average line profiles of the EBIC maps indicate maximum current generation and collection is at the device p-n junction; however, with the more defected device, the onset of collection is more delayed than the pristine device. Furthermore, the intensity of PbS 45 is half of that of PbS 43, corresponding to the halved J_{SC} value (Table 4.1). The EBIC signatures suggest that the interface of the device successfully generates EHPs, but PbS 45 displays limited charge transport through the PbS layer. This could mean that the electron mobility in the QD layer is poor due to the presence of shallow traps; the hole mobility, on the other hand, is maintained throughout both devices as indicated by

PbS 45's EBIC profile peak near the PbS / TiO_2 junction. The introduction of these recombination centers severely decreased the J_{SC}, thus the efficiency, due to the limited diffusion length of the charge carriers.

4.3.3 Improving efficiency via layer thicknesses

A means in which the pristine device was altered to improve the efficiency included the modification of the device layer thicknesses, i.e. PbS nanocrystals (monodisperse) and TiO_2. Based on the initial analysis of the "pristine" device, it was observed that there was EBIC signal originating several hundred nanometers within the TiO_2 layer; therefore, decreasing the thickness of the titania could potentially benefit the charge generation and collection by decreasing the pathway the electron must take to reach the cathode.

As a result of these changes, optimal PbS and TiO_2 layer thicknesses were found, thus producing a higher efficiency device. The maintained surface area of the moderately porous TiO_2 allows the charges from the QDs to more readily separate and become transported to their respective electrodes would attribute to the increased efficiencies. Based on the conclusions drawn from the prior section, the hole mobility is highly efficient; therefore, infiltration of the QDs into the TiO_2 would increase the efficiency. However, there is a notable decrease in the shunt resistance (R_{sh}) and increase in the series resistance (R_s) for the thinner TiO_2 devices, which attributes to the overall lower fill factors (Table 4.1).

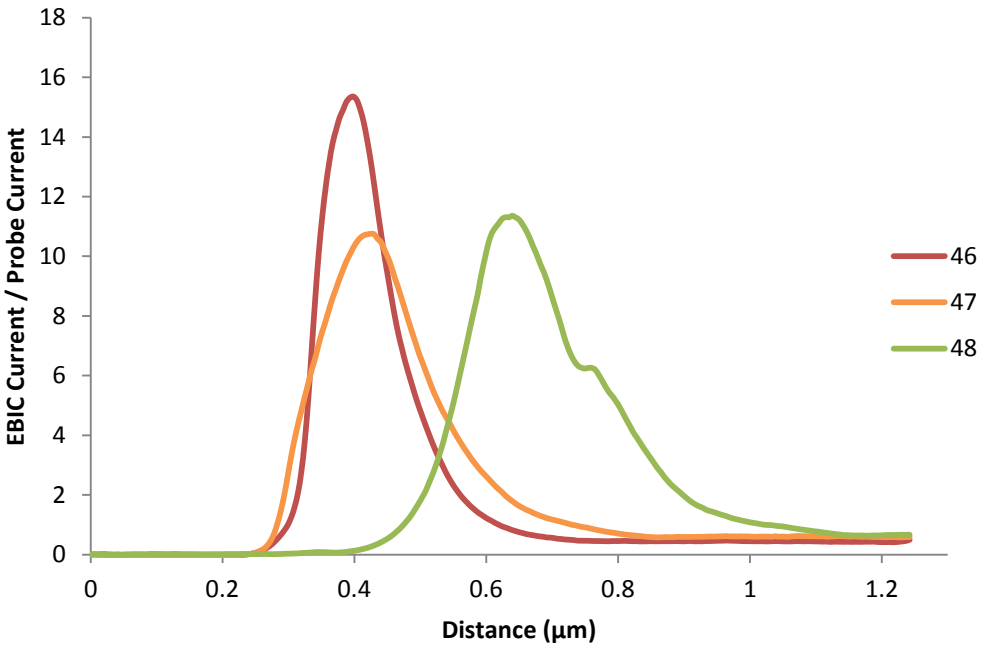

Figure 4.5 EBIC line profiles of PbS 46, 47, and 48.

The shapes of the average line profiles indicate that the thicker the PbS layer, the farther into the TiO_2 the signal extends. With a thicker active layer (~400 nm, sample 48), the electrons have a greater possibility of recombining before they reach the FTO; this would allude to poor hole conductivity. The p-n junction remains intact at the QD / titania interface for all the differing PbS thicknesses. In Figure 4.5, average line profiles display the shifts of the p-n junction (peak) in relation to the distance from the Ag / Au contact, which is at the zero on the x-axis. These shifts are more pronounced for PbS 47 and 48 as the difference in thickness for the layers can be found simply by measuring the distance between the peaks (~200 nm). With PbS 46, this is not the case due to the thinner QD layer; as opposed to 48, the entire PbS layer is depleted leading to a more

abrupt decay at the PbS / TiO_2 interface. PbS 47, which possessed the highest efficiency among all of the devices studied, displays a broader EBIC signal that spans the entire QD layer, suggesting complete depletion, as well as a gradual decay at the p-n junction.

4.4 Conclusions

In this study, a comparatively higher efficiency device was fabricated based on the correlative EBIC and STEM EDS data obtained. With initial studies of a literature-based device, noted as "pristine," features such as intermixing of the PbS and TiO_2 layers were found to exist. By using this information, optimal device fabrication parameters were elucidated and applied to make a higher efficiency photovoltaic device. SEM EBIC can aid in the determination of depletion regions and locations of p-n junctions, but the addition of STEM EDS, confirms the nanoscale details unable to be observed with SEM. The method of characterization presented here proves that it can reveal important information of sub-1 μm thick photovoltaic devices.

CHAPTER V

TITANIA NANOTUBE QUANTUM DOT-BASED PHOTOVOLTAIC DEVICE CHARACTERIZATION VIA FIB AND STEM EDS

5.1 Introduction

Michael Grätzel and Brian O'Regan first introduced the dye-sensitized solar cell in 1988.[86] The novelty of this device, in comparison to what was already available, is its application of an organic component with the ability to generate electron-hole pairs readily; with the assistance of a titania layer, those charges could separate and be harvested for electricity. Over the course of several years, this device made a significant impact in the field of photovoltaics as this was a low cost alternative to the expensive silicon-based technology.

Currently, the record efficiency for this type of solar cell is approximately 12% and has lingered at that value for about 15 years. The scientists working in the field (Grätzel included), realized it was time to switch gears. At first, the idea to keep the dye component and alter the TiO_2, proved to be somewhat successful. Instead of using a spherical nanoparticulate layer of the titania, they were replaced with various shapes, such as hyperbranched structures,[87] nanowires,[88,89] and tubes.[37–39,90] However, there was another problem: the degradation of the organic dye over time. In addition to that factor, the use of electrolytes in the device also generated more issues in the commercialization of this architecture.

Serendipitously, quantum dots (QDs) made their foray into the nanotechnology realm at around the same time. Due to the inherent ability of these colloidally synthesized nanocrystals to create electron-hole pairs by excitation via photons, they seemed like a perfect substitute for the unstable dye. This, however, proved to be more difficult than predicted. For years, the efficiencies suffered due to the ligands impacting the charge collection among numerous other factors.[11,81] Recently, in 2010, Pattantyus-Abraham et al, found a way to achieve upwards of 5% efficiency.[32]

Figure 1.7 shows the architecture of interest for this section. The proposed pathway of the charge carrier movement: the electrons and holes would be generated at the PbS quantum dots, then separated, where the electrons would be swept to the TiO_2 and then to the Ti foil, while the holes would percolate to the ITO. This architecture mimics that of the Grätzel/dye-sensitized cell in that it utilizes TiO_2 as an intermediate in the charge separation process as well as using an EHP generator (dye vs. quantum dot). The device in Figure 1.7 modifies the components of the traditional dye-based cell so that charges are more readily produced and separated while being a completely solid-state solar cell.

Depth of QD penetration becomes very important to the performance of this device. With PbS nanocrystals filling farther into the hollow titania nanotubes, this allows for a greater surface contact to create a tunnel for the electrons to flow to the cathode. This is a challenge as the tubes are still attached to the Ti foil. One of the problems is determining how far the QDs fill the nanotubes.

Presented here is a means to characterize the QD filling depth using a controlled method of preparation and high resolution elemental analysis. In the past, scraping the sample and performing SEM EDS would be the best technique or worse, simply making the determination by appearance.[42,91] Both of these methods can be inconsistent, as some of the sample could shatter at different regions of the tubes and not be representative of the sample.

5.2 Experimental

Quantum dot fabrication and device fabrication information are explained in detail in Wrenn et al.[91] Briefly, PbS QDs are synthesized and filled into the anodically prepared TiO_2 nanotubes via 3-mercaptopropionic acid (MPA) ligand exchange. The efficiency for this particular device is 0.003%.

The FIB process was performed using extreme care as TiO_2 is very susceptible to uncontrolled ion beam interactions/damage. By using low probe currents, the sample was preserved as much as possible during the final polishing steps. As stated in detail in Sections 2.5.2 and 2.5.3, initial trenches were milled at the front, back, and left of the region of interest by using the Lyra3. The following was done with the Auriga: (1) thinning of the lamella to 300 nm, (2) partially releasing the section, (3) attaching it to the Kleindiek and then the lift-out grid post. Once again, for the final polishing steps of the process, low probe currents (<100 pA) were used.

5.3 Results & discussion

This technique provides straightforward data with little room for misinterpretation. In summary, the PbS QDs, as expected, mostly sit at the tops of the tubes due to the difficulty of filling a closed tube structure; however, upon closer inspection of the scanning transmission electron microscope (STEM) EDS maps, distribution of the PbS QDs is throughout the length of the tubes, visible up to 4 μm in this lift-out sample; however, the coverage is less than uniform. Also based on the EDS maps, the ITO covers the surface of the tubes while very little has infiltrated the inner portion of the titania. This would lead to limitations in the hole transport mechanism to a certain extent, thus leading to lower efficiencies.

Furthermore, with images taken at high magnification (aberration-corrected STEM), there is evidence that the nanotubes have a coating of a substance, which appears to be a layer of organics or unreacted precursors (Figure 5.2). Due to the use of MPA to cross-link the PbS QDs, residual S and C could be present and generate a signal farther into the tubes than where the QDs are actually present. If there is residual S-based organics lining the tubes, there is a chance that it could be influencing the Pb signal as the two tend to overlap in EDS spectra. This would either suggest that the organic molecule, is infiltrating farther into the nanotubes than the QDs or the PbS is truly providing complete coverage of the TiO_2.

5.4 Conclusion

Presented here is a technique in which to study QD-based nanotube-structured photovoltaic devices. Sample preparation must be done with care, however the data acquisition is fast and important information can be concluded from the maps and images. In this case, it was found that the PbS does not uniformly coat the nanotubes, at the same time, the ITO does not penetrate the tubes farther than 50 nm. Both of these factors combined could attribute to the low efficiency of this device. A means to alleviate the problems includes overwhelming the titania with QDs to ensure the coating of PbS is to be uniform; however, this may prevent the ITO from infiltrating the tubes as there is already a barrier of PbS QDs from the data acquired. Other routes must be taken to resolve these issues.

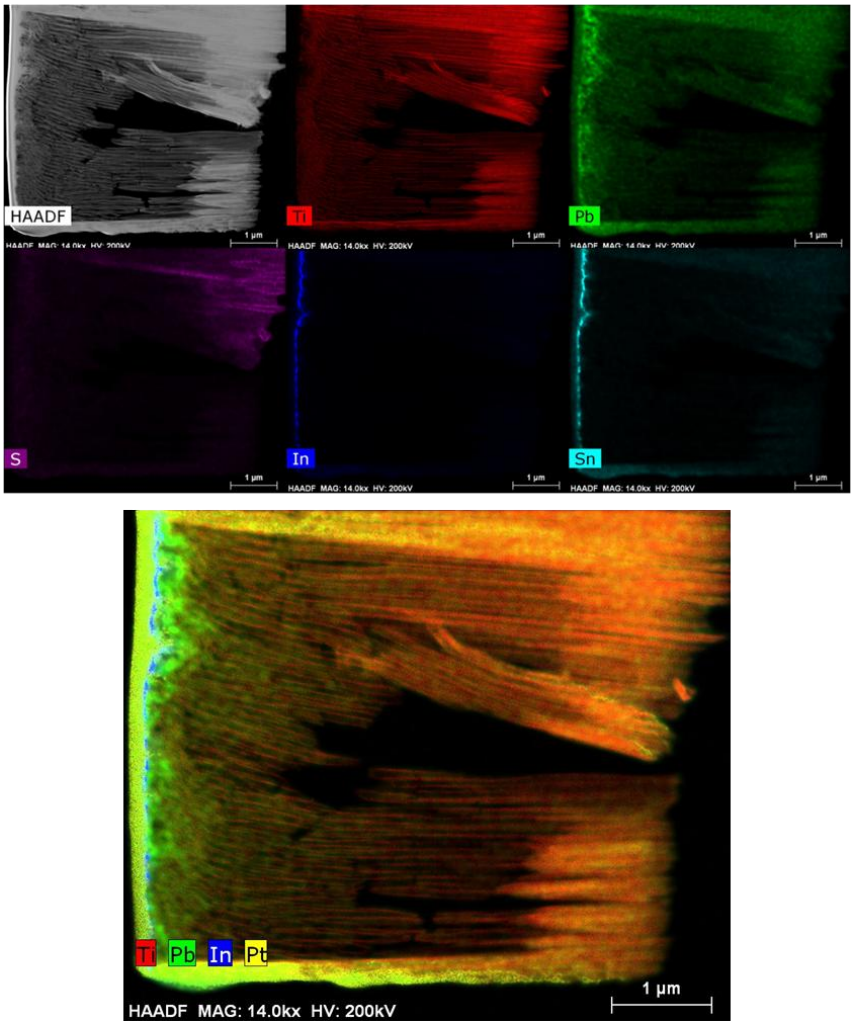

Figure 5.1 STEM EDS data of the TiO_2 nanotubes decorated with PbS QDs and coated with an ITO layer anode. PbS is found to be distributed along the entire lamella, however, it is not uniform, with a large concentration of dots forming a layer at the upper end of the nanotubes. ITO evenly coats the tops of the tubes due to the layer of PbS blocking further infiltration.

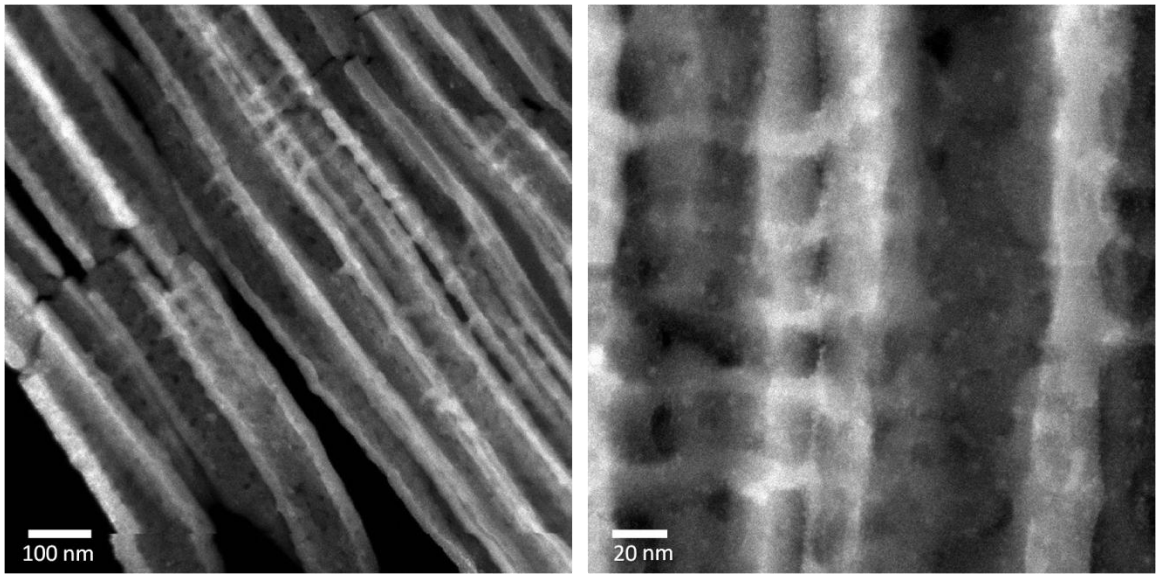

Figure 5.2 STEM images of the TiO_2-PbS device showing (on the right image) a coating on the tubes along with specks that could be the PbS QDs.

CHAPTER VI

PRELIMINARY: C_S-STEM EBIC OF A PHOTOVOLTAIC DEVICE

6.1 Introduction

As shown in Chapters III and IV (and Appendix D), SEM EBIC is a powerful tool used to investigate the electronic activity of solar cells. One of the major limitations to the method is the resolution. The small scale nature of the devices being studied makes the probing of the nanoscale defects more difficult in SEM.

The ultimate goal of all the EBIC culminates to aberration-corrected STEM EBIC, a feat never accomplished before. Cs-STEM EBIC would allow an individual to simultaneously image structure at near-atomic resolution while also generating an electronic properties map. With an ongoing project from the SunShot Initiative (U.S. DOE), CdTe thin film devices are of particular interest in this portion of the work. Furthermore, this type of device is much more straightforward to analyze than a quantum dot-based one.

6.2 Experimental method

Sample preparation was developed by Dr. Jonathan Poplawsky. In short, a sandwich cross-section of the sample was made and glued onto a gold quadrant TEM grid, where the center of the grid has been pierced with a sharp point (essentially, a larger hole in the middle is made). In order to make the anode and cathode contacts,

ion beam induced wires were deposited from the sample to the Au pads of the TEM grid, respectively. This connected sample was then placed onto a PCB chip fit for the biasing holder on the UltraSTEM (see next paragraph); the PCB chip has six gold pads (three on the top, and three on the bottom) which correspond to connectors for the sample holder Figure 6.1. Thin pieces of wire and silver paste were used to make the connections from the Au grid to the PCB chip.

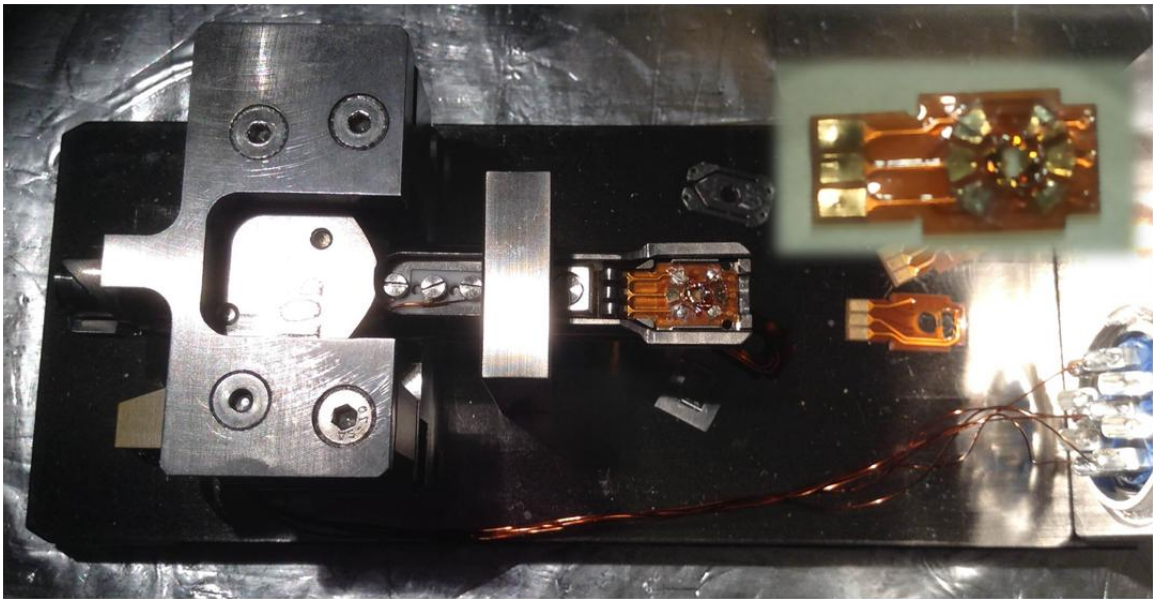

Figure 6.1 Nion UltraSTEM electrical/biasing holder with PCB chip inserted into holder. The inset is a close-up of the PCB chip.

The EBIC system is a pseudo-homebuilt one where the SEM EBIC current amplifier (Gatan, commercial) was taken and adapted to the Nion UltraSTEM 200 feed-throughs. The sample holder is the standard biasing/electrical holder available with the

UltraSTEM; this holder has six spring loaded “probes” that make contact to the PCB chip, which then lead to the sidewall of the cartridge. These connections on the side of the cartridge make the appropriate contacts on the feed-throughs on the microscope.

6.3 Preliminary results

Using CdTe as the platform, preliminary data was collected via Cs-STEM EBIC. As shown in Figure 6.2, the simultaneous HAADF and EBIC are taken at two different magnifications emphasizing the small scale characteristics of the CdTe / CdS interface. Features down to a resolution of about 50 nm can be seen. For instance, in the lower set of HAADF and EBIC images, the shape of the CdTe layer is followed in the EBIC signature. The images shown are raw data without correcting for aberrations. Although this is preliminary data, there is much promise in the technique.

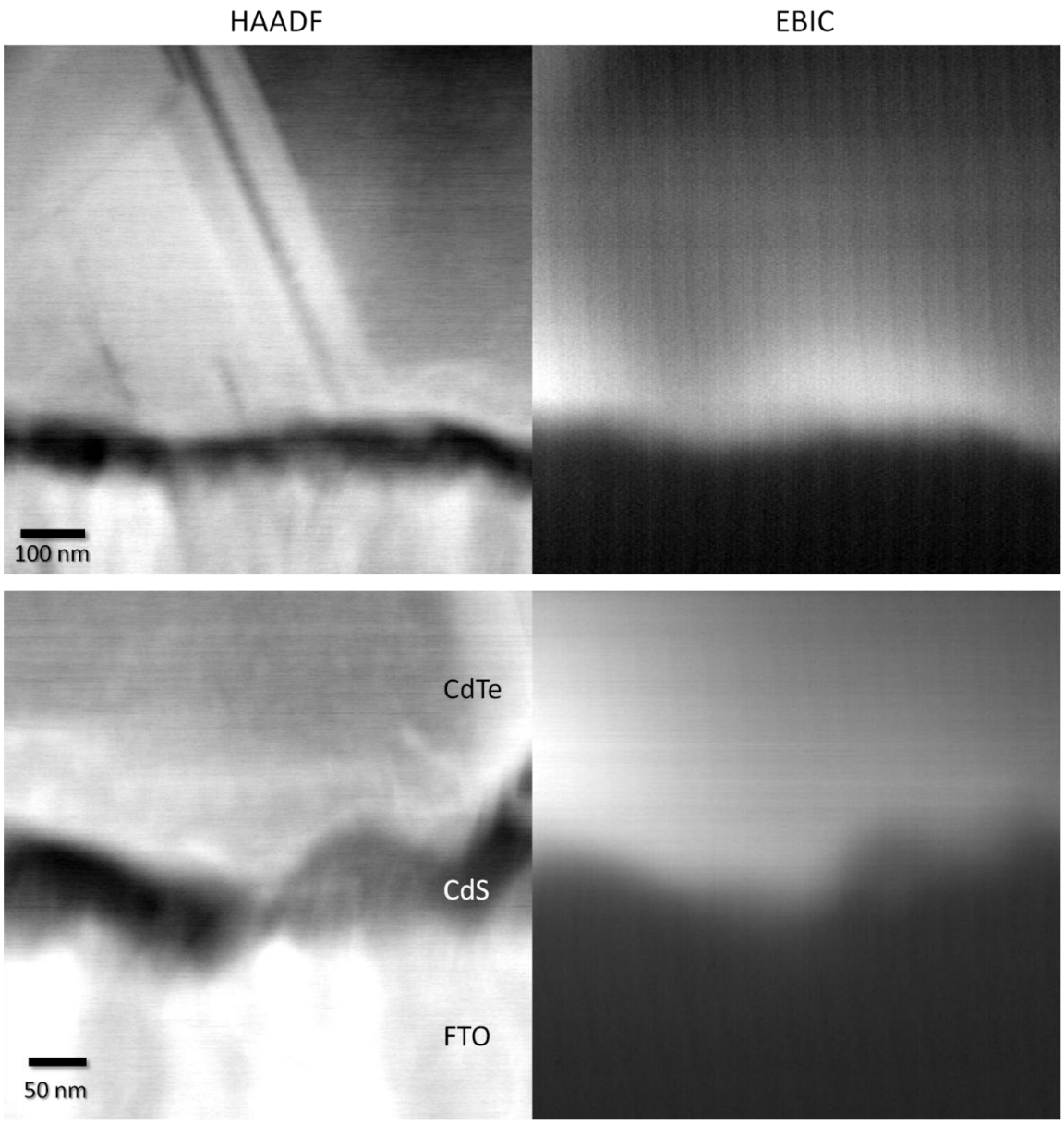

Figure 6.2 The obtained HAADF and simultaneous EBIC images of a CdTe thin film PV sample. In the lower set of images, the EBIC clearly shows a contoured shape to the CdTe active layer.

CHAPTER VII

SYNOPSIS & CONCLUSIONS

The work presented in this thesis demonstrates a new ability to characterize nanocrystal-based photovoltaic technologies. Using techniques such as electron beam-induced current and scanning transmission electron microscopy, unprecedented information was extrapolated in regards to three different architectures. This is the first time EBIC has been utilized to study this type of third generation solar cell.

First measured was a bulk heterojunction device, CdSe:P3HT, that suffered from low efficiencies due to the fact that only the nanorods interfacing the cathode had the ability to transport electrons; at the same time, the holes were determined to be far more mobile than the electrons (Chapter III). Second measured was a PbS quantum dot depleted-heterojunction solar cell that showed unexpected intermixing of the QDs with the TiO_2 layer for several hundred nanometers, which resulted in a decaying p-n junction. Furthermore, when defects were introduced into the device, EBIC was able to detect them. An improved device was fabricated based upon the information gathered from the initial experiments (Chapter IV). Last was a characterization method for a PbS QD-infiltrated titania nanotube device. It was shown that this device has potential in that the PbS filling the nanotubes penetrated farther into the tubes than expected, thus the ability to achieve higher efficiencies is possible; albeit it will be difficult to apply

enough nanocrystals to effect significant outcomes/efficiencies without creating a barrier for the conductive oxide layer (Chapter V).

Preliminary work on combining EBIC and Cs-STEM was also presented on a thin film CdTe photovoltaic (Chapter VI). The ultimate goal is to apply the method to nanocrystal-based devices to better understand the near-atomic electronic properties of the solar cells. Ideally, the studies will provide insight into the areas in need of improvement, such as synthetic routes for the quantum dots (individual QD defects) or fabrication techniques for the devices (interfacial concerns).

Through these investigations, there proves to still be hope for nanocrystal-based photovoltaics to be a competitive form of technology in the future. With a more thorough understanding of the system, the theoretical efficiencies of these devices, which are significantly above the Shockley-Queisser limit for more traditional cells, are much closer to being obtainable. Further development of nanocrystal-based photovoltaics, and solar cells in general, will help to produce greener, more efficient means of energy to fuel the demands of an ever-growing population.

APPENDIX A

CALCULATING DEVICE EFFICIENCIES

The efficiency of a solar cell is one of the most important factors in studying how well it is performing. Despite the availability of programs that can calculate all the relevant parameters (i.e. efficiency, open circuit voltage, short circuit current, fill factor, etc.) for a given device, it is always beneficial to know how to do it "by hand." Before proceeding with the graphing of acquired data, there are two equations and a figure one must understand:

$$P_{max} = V_{OC} I_{SC} FF \tag{A.1}$$

$$\eta = \frac{P_{max}}{P_{in}} \tag{A.2}$$

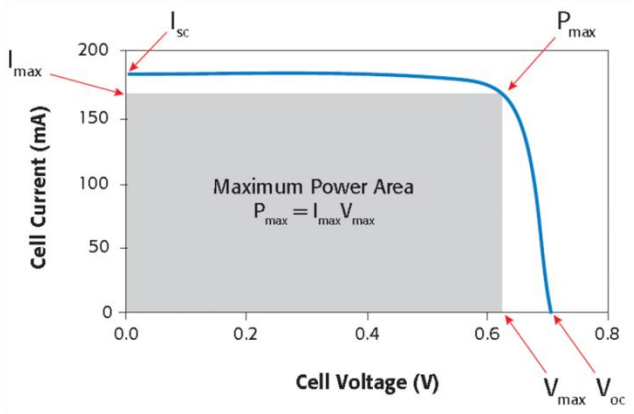

Figure A.1 An ideal I-V curve.

In Figure A.1, each parameter of interest is labeled on an ideal I-V curve. As can be seen, all the factors are related, and they all impact the overall efficiency, η. P_{in} is calculated by multiplying the measured area of interest (usually a metal pad contact) in cm^2 and the calibrated solar simulator system so that the device being tested achieves 1000 W/m^2, or approximately one sun, irradiation. The other components will be found in the following section.

First, one must acquire the voltage-current data via a Keithley sourcemeter and program that logs both components while doing a sweep. Taking the resultant current and plotting it against the voltage, an I-V curve is obtained. The curve, however, is in the fourth quadrant; it should be in the first so that the different parameters can be calculated more easily (this example is done in Excel, but other programs can be used). The way to shift the graph is to simply multiply the current value by negative one. Once this is done, adjust the axes so that the intersection of the curve with the x-axis and y-axis are "magnified" (Figure A.2).

In order to obtain P_{max}, one should multiply the voltage by the current (negative) and find its maximum. With P_{max}, the corresponding I_{max} and V_{max} can be found, if desired. At this point, the efficiency can be calculated by dividing P_{max} by P_{in}.

Last is the fill factor. To find the FF, both the V_{OC} and I_{SC} must be found first. These are easy to find as they are where the current is equal to zero and voltage is zero, respectively. As can be seen in Figure A.3, the FF is simply the P_{max} divided by the product of the V_{OC} and I_{SC}.

	A	B	C	D	E	F	G	H	I	J	K	L	M	N	O
1	Voltage	3.11E-06	1.01E-02	2.02E-02	3.03E-02	4.04E-02	5.05E-02	6.06E-02	7.07E-02	8.09E-02	9.09E-02	1.01E-01	1.11E-01	1.21E-01	1.31E-01
2	Current	-2.24E-04	-2.21E-04	-2.21E-04	-2.19E-04	-2.18E-04	-2.17E-04	-2.16E-04	-2.15E-04	-2.15E-04	-2.13E-04	-2.11E-04	-2.09E-04	-2.07E-04	-2.06E-04
3															
4	Voltage	Current	Neg Current												
5	3.11E-06	-2.24E-04	2.24E-04												
6	1.01E-02	-2.21E-04	2.21E-04												
7	2.02E-02	-2.21E-04	2.21E-04												
8	3.03E-02	-2.19E-04	2.19E-04												
9	4.04E-02	-2.18E-04	2.18E-04												
10	5.05E-02	-2.17E-04	2.17E-04												
11	6.06E-02	-2.16E-04	2.16E-04												
12	7.07E-02	-2.15E-04	2.15E-04												
13	8.09E-02	-2.15E-04	2.15E-04												
14	9.09E-02	-2.13E-04	2.13E-04												
15	1.01E-01	-2.11E-04	2.11E-04												
16	1.11E-01	-2.09E-04	2.09E-04												
17	1.21E-01	-2.07E-04	2.07E-04												
18	1.31E-01	-2.06E-04	2.06E-04												
19	1.41E-01	-2.03E-04	2.03E-04												
20	1.52E-01	-2.02E-04	2.02E-04												
21	1.62E-01	-2.00E-04	2.00E-04												
22	1.72E-01	-1.98E-04	1.98E-04												
23	1.82E-01	-2.01E-04	2.01E-04												
24	1.92E-01	-1.96E-04	1.96E-04												
25	2.02E-01	-1.94E-04	1.94E-04												

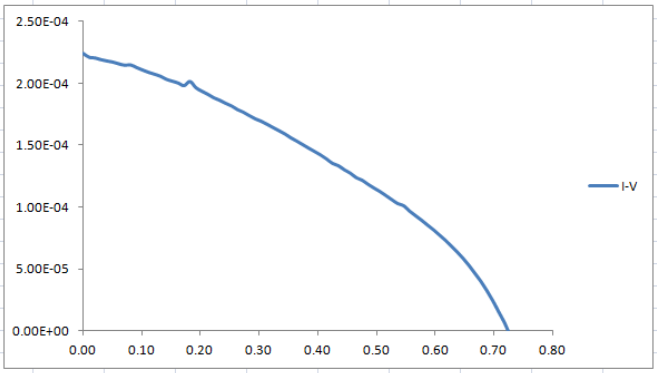

Figure A.2 The negative of the current is graphed with the voltage. The axes are adjusted so that the intercepts of the x- and y-axes are expanded.

N24 =H22/(K24*K26)

	A	B	C	D	E	F	G	H	I	J	K	L	M	N	O
4	Voltage	Current	Neg Current	Power (I*V)											
5	3.11E-06	-2.24E-04	2.24E-04	6.96E-10											
6	1.01E-02	-2.21E-04	2.21E-04	2.23E-06											
7	2.02E-02	-2.21E-04	2.21E-04	4.45E-06											
8	3.03E-02	-2.19E-04	2.19E-04	6.64E-06											
9	4.04E-02	-2.18E-04	2.18E-04	8.81E-06											
10	5.05E-02	-2.17E-04	2.17E-04	1.10E-05											
11	6.06E-02	-2.16E-04	2.16E-04	1.31E-05											
12	7.07E-02	-2.15E-04	2.15E-04	1.52E-05											
13	8.09E-02	-2.15E-04	2.15E-04	1.74E-05											
14	9.09E-02	-2.13E-04	2.13E-04	1.93E-05											
15	1.01E-01	-2.11E-04	2.11E-04	2.13E-05											
16	1.11E-01	-2.09E-04	2.09E-04	2.32E-05											
17	1.21E-01	-2.07E-04	2.07E-04	2.51E-05											
18	1.31E-01	-2.06E-04	2.06E-04	2.70E-05											
19	1.41E-01	-2.03E-04	2.03E-04	2.88E-05											
20	1.52E-01	-2.02E-04	2.02E-04	3.06E-05											
21	1.62E-01	-2.00E-04	2.00E-04	3.24E-05											
22	1.72E-01	-1.98E-04	1.98E-04	3.40E-05			Pmax	5.79E-05		Pin	0.0072		% Eff	0.80%	
23	1.82E-01	-2.01E-04	2.01E-04	3.66E-05											
24	1.92E-01	-1.96E-04	1.96E-04	3.77E-05			Vmax	4.44E-01		Voc	0.722		FF	3.58E-01	
25	2.02E-01	-1.94E-04	1.94E-04	3.91E-05											
26	2.12E-01	-1.91E-04	1.91E-04	4.05E-05			Imax	1.30E-04		Isc	2.24E-04				
27	2.22E-01	-1.88E-04	1.88E-04	4.19E-05											

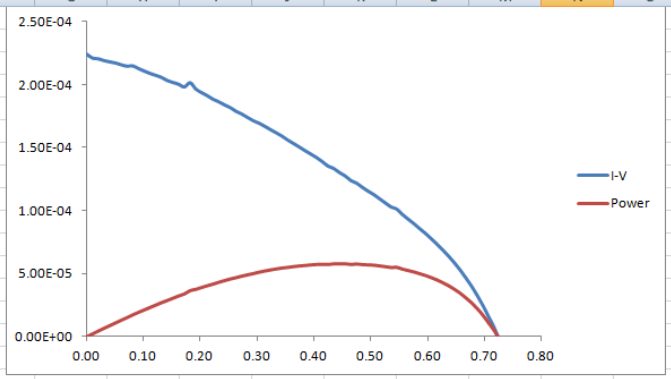

Figure A.3 Finding all the parameters necessary for calculating the efficiency and fill factor.

APPENDIX B

SYNTHESIS OF CDSE NANOCRYSTAL MORPHOLOGIES

B.1 Spherical

There are two means to synthesize spherical CdSe nanocrystals; phosphonic acid-based and oleic acid-based. They each yield different crystal structures, being the former produces wurtzite, while the latter gives zinc blende. The synthesis is adapted from prior published work.[19,92]

B.1.1 Wurtzite

In a 50-mL three neck round bottom flask, 10 g of TOPO and 10 g of HDA were loaded. Additionally, the DDPA (1.00 g, 4 mmol) and CdO (0.256 g, 2 mmol) were carefully transferred to the vessel. Fitted with a Teflon collar at the center neck, a self-washing bump trap was securely fastened and the top of the bump trap was a connection to the argon line. On the left neck, a clean thermocouple was positioned so that the tip of the probe barely touched the bottom or sidewall of the flask. The right neck was fitted with an appropriately sized serrated rubber septum, used for purging the system as well as injecting the Se precursor.

The flask was then heated to 150°C while purging with a needle; the needle was then removed at that temperature and the flask continued to heat to 330°C. Once the contents of the flask "convert," or become a clear solution, a 0.2 M solution of Se

powder dissolved in TBP, was injected in an 8 mL quantity. The solution was maintained at a temperature of 260°C for growth of the nanocrystal size. Once the desired size was attained, the heating mantle was removed and the flask was cooled using a direct stream of compressed air.

At about 90°C, the colored solution was transferred to centrifuge tubes (six or more) in equal amounts. The nanocrystals were then doused with methanol to fill the remainder of the centrifuge tube. These were then centrifuged at 6000 rpm for 3 minutes, after which the supernatant was discarded and the precipitate dried, inverted on a paper towel. Octanol, in 5 mL amounts for each centrifuge tube, was added and agitated until the pellet completely dissolved into the solvent. These tubes were centrifuged again for 20 minutes at 6000 rpm. The supernatant that consisted of the clean nanocrystals were transferred to clean centrifuge tubes, at which methanol was added to flocculate the nanocrystals. Once again, the tubes were centrifuged at 6000 rpm for a final time. The supernatant from this last wash was discarded, and the centrifuge tubes were inverted onto paper towels to dry. The resultant dry pellet was solubilized into toluene, or solvent of choice, e.g. hexane, chloroform.

A variation of this synthesis includes shooting a smaller amount of the 0.2 M Se:TBP solution to achieve larger nanocrystals in a shorter period of time. Another would be the changing of the ratio between TOPO and HDA.

B.1.2 Zinc Blende

Similar to the wurtzite synthesis, CdO precursor (2 mmol, 0.256 g) was added to the reaction vessel with surfactants, in this case oleic acid (~8 mmol, 2.4 mL) and non-coordinating solvent, ODE (10 mL). The flask was heated to 250°C with Ar purging (to 150°C) until the solution is clear. Reaction flask was cooled to add 1.5 g octadecylamine and 0.5 g TOPO; system was reheated and re-purged to 230°C. A prepared solution of 1 mL of 1.5 M Se:TBP was swiftly injected at 200°C and the nanocrystals were allowed to grow until the desired size at 190°C. Flask was then cooled to 90°C with compressed air.

With a mixture of methanol and butanol, the nanocrystals were precipitated and then centrifuged at 6000 rpm for 20 minutes. Once the supernatant was removed, minimal amounts of chloroform were added to the centrifugation tubes to solubilize the nanocrystals; acetone was used to precipitate the nanocrystals by filling the remainder of the tubes. This last step was repeated once more, and the dried nanocrystals were dispersed in the desired solvent.

B.2 "Tetrapods"

The synthesis of the tetrapods is similar to the synthesis of the spherical wurtzite CdSe, with some changes. Surfactants of TOPO (5 g) and DDPA (2 mmol, 0.50 g) were added to a 50-mL round bottom flask, along with 1 mmol (0.128 g) of CdO. This flask was then purged through with ultrahigh purity Ar, while being heated to 310°C. During the temperature ramp, a carboxylic acid (acetic (2-10 mmol), hexanoic, or octanoic acid) was injected into the flask. As the Cd complexes with the phosphonic acid and

carboxylic acid, the pot becomes cloudy white/beige. Upon reaching the temperature set-point, 4 mL (0.8 mmol) of a 0.2 M Se:tributylphosphine solution was swiftly injected. The nanocrystals were allowed to grow at 260 °C for one hour. The nanocrystals were cooled and then precipitated with methanol; centrifugation separated the excess precursors from the product. This procedure varied from a spherical nanocrystal synthesis by the addition of the carboxylic acid and the removal of HDA to assist in inducing the elongated morphology. The synthesis yields mostly tetrapods, but also mixed in with rods, bipods, and tripods.

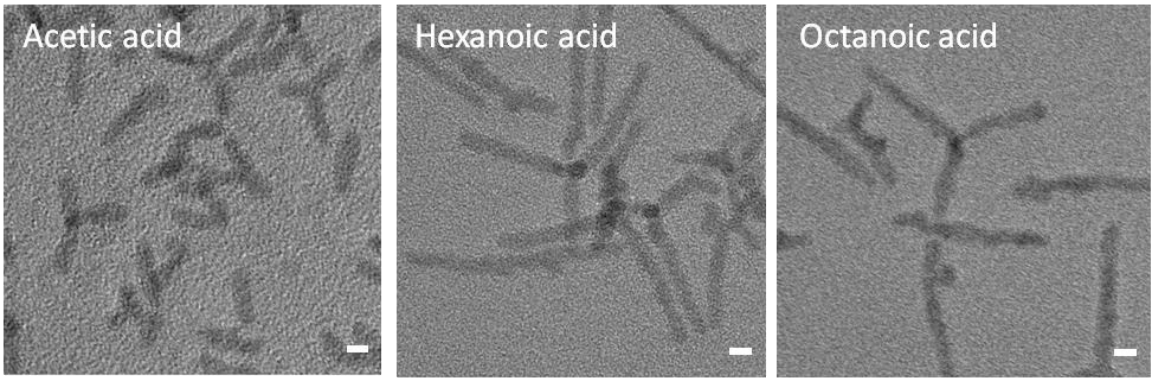

Figure B.1 Different carboxylic acid-induced tetrapod formation. The scale bar is 5 nm.

APPENDIX C

ELECTRICAL CHARACTERIZATION OF IBID TUNGSTEN WIRES FOR STEM EBIC

C.1 Introduction

The ability to electrically characterize micro- and nano-scale structures has been a limiting factor for advancements in the field of ion beam induced deposition (IBID). Due to the small size of these deposits, traditional electrical testing methods utilizing micrometer-sized probes would not be practical.[93]

More recent platforms that are used to test micro- and nano-structures involve, for example, a thermally deposited gold pad onto electron transparent membranes,[94] employing scanning tunneling microscope probes,[95] or simply depositing additional wires/electrodes to transport charges.[96] With electrical characterizations of *in situ* two- and four-point probe measurements, the quality of IBID fabricated structures can be determined; however differences in types of platforms and substrates introduce a plethora of inconsistencies and variables. Presented here is a new approach using an *in situ* MEMS-based electrical testing technique to determine whether as-deposited IBID tungsten wires formed Ohmic contacts to a commercially manufactured silicon nitride (Si_3N_4) substrate and gold pads. Further materials characterization was performed to determine sheet resistivity, elemental composition, and structure of the as-deposited wires.

The work provided here allows STEM EBIC preparatory steps to be achieved in high quality. In addition to making a sample that is electron transparent, the connections between the cross-section and the remainder of the substrate (see the schematic in Figure C.1) must be well constructed as well as be on the nanoscale size regime. For the latter reason, FIB was chosen as the method of deposition due to the ability to create fine structures in a very controllable manner.

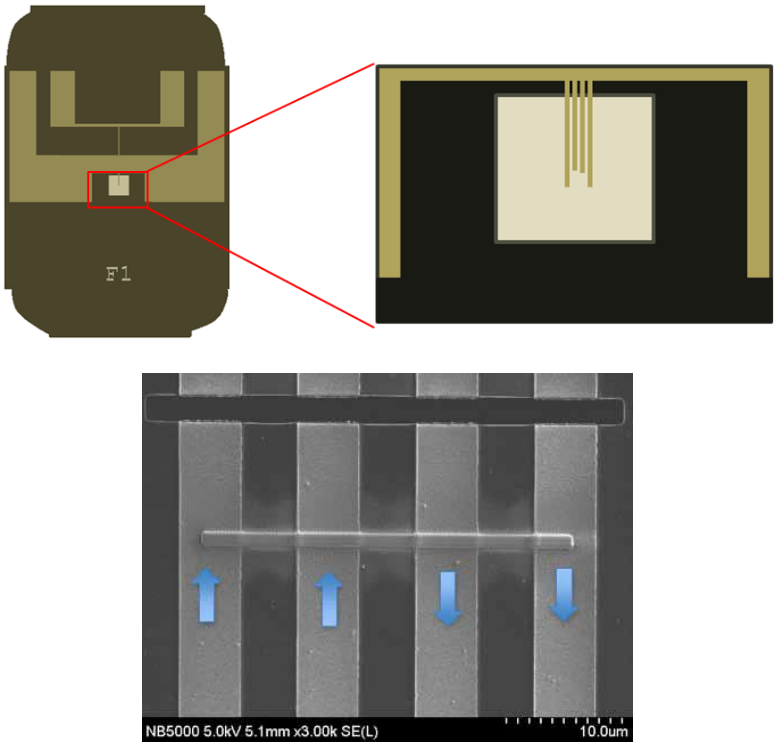

Figure C.1 Protochips Aduro platform and 4-pt probe configuration where the voltage is measured on the inner two leads while current is induced.

In order to determine if the connections deposited by focused ion beam are Ohmic, initial studies were conducted using the aforementioned method will be used. On a Protochips Aduro MEMS-based e-chip (Figure C.1, Raleigh, NC), the optimal parameters for depositing tungsten wires were determined by I-V measurements. Using the four gold leads on the Aduro, the four-point-probe measurements were conducted.

C.2 Experimental methods

The W wires were deposited via $W(CO)_6$ gas precursor with a 40 kV ion beam at 70 pA using a Hitachi NB5000 FIB/SEM facilitated by Ga^+ ions. Energy dispersive x-ray spectroscopy (EDS) was taken of the deposited wire on the gold pads of the Aduro platform (Figure C.2). The IBID W wire measured 30 µm in length and 1 µm in width. Using AFM, the thickness of the wire was determined to be 200 nm.

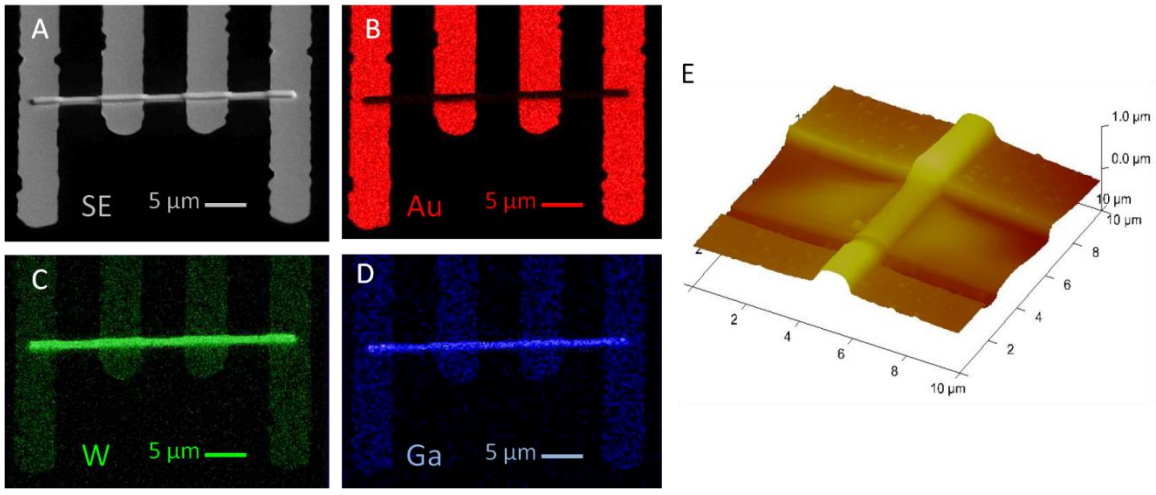

Figure C.2 SEM EDS maps of the deposited wire, (A) – (D), as well as AFM to determine the thickness of the IBID wire.

To conduct the four-point-probe studies, two Keithley 3400 source meter units were employed; one to source the current, the other to measure the voltage.

C.3 Results & discussion

Current-voltage measurements were taken of three different IBID tungsten wire samples (Figure C.3). A current was swept to detect the voltage produced as a result of the wire. The resistivity was calculated from the measured resistance; this value was compared to the resistivity of a sheet of tungsten.

$$\rho = R\frac{A}{l} \tag{C.1}$$

The equation takes into account the area of the wire cross-section (*A*), the length of the wire, *l*, and the resistance, *R*. Taking the average of the three as-deposited wires' resistances (27 Ω), the resistivity was determined to be between 50 and 51 μΩ cm. In comparison to bulk tungsten (5.6 μΩ cm), there is only a one magnitude difference.[97]

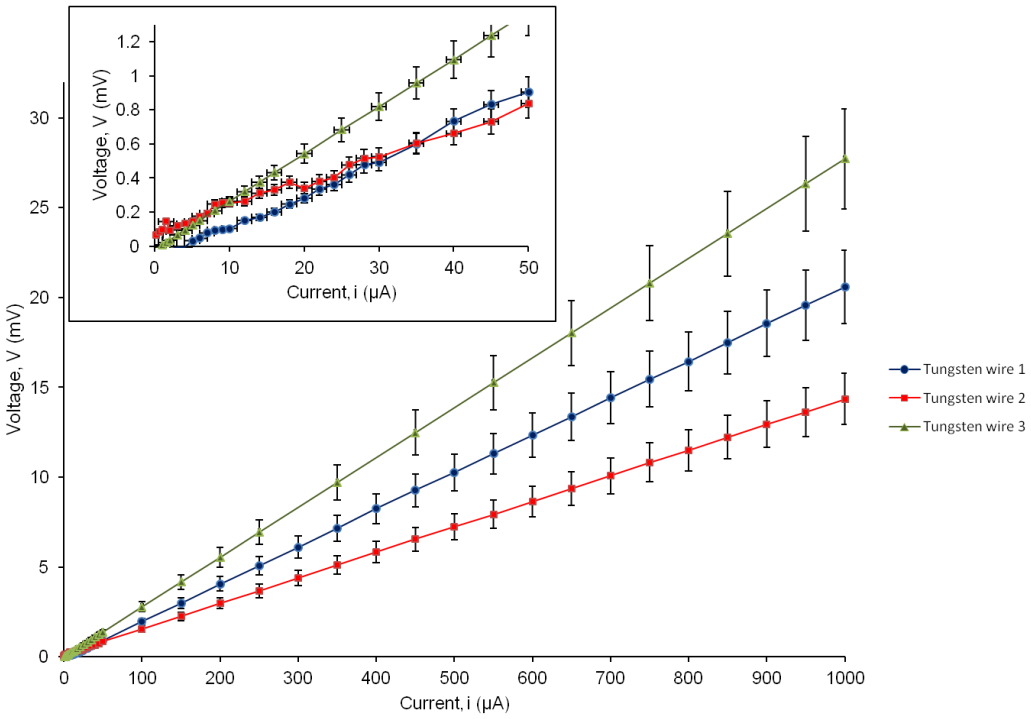

Figure C.3 I-V traces of three sample tungsten wire deposits.

C.4 Conclusion

The as-deposited wires, despite from a FIB, are Ohmic and provide a high quality means of connecting the cross-sectioned sample to the STEM EBIC platform. The Aduro stage also demonstrates its ability to characterize the electrical properties of FIB deposited wires.

APPENDIX D

SEM EBIC OF CDTE THIN FILM SOLAR CELLS

D.1 Introduction

Second generation solar cells completely changed the playing field when it came to materials cost vs. performance. With traditional Si-based photovoltaics, very thick layers of active material (hundreds of micrometers) were necessary for the proper functionality of the devices; however, with the advent of CdTe and CIGS, the thicknesses were reduced significantly to less than 10 µm. One can use less material, but if the efficiency doesn't compare, then the effort is for naught. As of October of 2014, First Solar holds the record efficiency of 21% for CdTe thin film solar cells, comparable to single crystalline silicon (~26%).

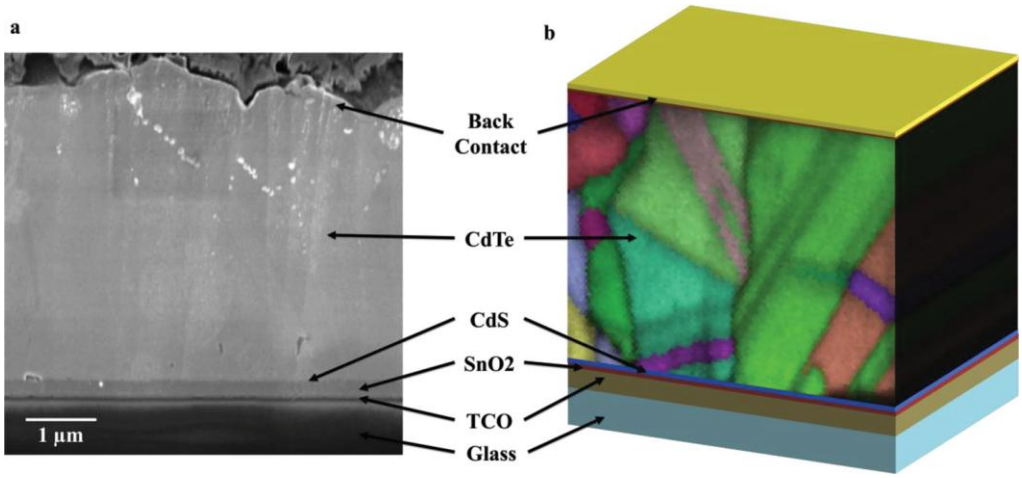

Figure D.1 Cross-section of the CdTe device from Poplawsky et al.[85] (A) shows a secondary electron micrograph of the device, while (B) indicates the grains along the CdTe layer.

As a promising technology, one must look for different ways to not only improve it, but also make it more "fabrication friendly." The typical route for making CdTe involves the use of highly toxic $CdCl_2$ during one of processing steps. Needless to say, means to avoid it would be ideal. So the question now: what is a good substitute for $CdCl_2$ that will preserve the efficiency and protect the manufacturers?

The work presented here serves to address that question. This step in the process is a necessity as determined by Li et al and Poplawsky et al therefore it cannot be bypassed; the important factor is the presence of Cl.[76,85] Cl segregation within GBs and at the CdS/CdTe interface dope the material to be n-type, which creates p-n junctions between the interfaces and p-type grains.[85] By using several different Cl-based salts, the CdTe was treated with CuCl, KCl, $MgCl_2$, NaCl, and $ZnCl_2$ instead of $CdCl_2$ to see what the effectiveness of each would be. In prior studies, it was shown that $MgCl_2$ made an positive impact toward the efficiency of the CdTe.[98]

D.2 Methods

The CdTe devices were fabricated and treated using $CdCl_2$ (standard), CuCl, KCl, $MgCl_2$, NaCl, and $ZnCl_2$ (un-published). Details can be found in their prior work.[99] The Cl-based heat treatments are introduced in the latter steps of the fabrication process.

As published by Poplawsky et al, the CdTe solar cells were cross-sectioned to reveal a polished edge for SEM EBIC analysis.[85] A completely topographically flat cross-section must be achieved for the best, most accurate EBIC results.

D.3 Results

Although none of the newly used Cl-based treatments did quite as well as $CdCl_2$, $MgCl_2$ and $ZnCl_2$ proved to be competitive alternatives, as shown in Table D.1. Looking at their electronic activity (EBIC maps, Figure D.2), both the Zn- and Mg-based salts appear to cause changes similar to the $CdCl_2$ treatment. Surprisingly, NaCl is also a viable option as its efficiency is still relatively high; however, the EBIC signature shows a reversal of the p-n junction. Instead of having the primary collection of the EHPs at the CdTe / CdS interface, the carrier collection occurs where the CdTe meets the back contact (refer to Figure D.1).

In Figure D.3, the EBIC average line profiles are compared; it shows the evolution of the device carrier separation properties with respect to the different treatments. For a standard device, most of the activity occurs within 1.5 µm from the CdS / CdTe junction. Both $ZnCl_2$ and $MgCl_2$ also showed this type of profile, however, it is less defined than the $CdCl_2$. The CuCl salt shows a similar initial peak as the standard, but it decreases quickly away from the interface. KCl displayed the weakest profile, where a peak appears at around 0.5 µm, but it does not increase. As mentioned before, NaCl is interesting in regards to the potential change in the doping levels of the material, thus changing the primary p-n junction location.

Table D.1 Efficiencies for all the Cl salt heat treatments.

Post deposition heat treatment	Voc (mV)	Jsc (mA/cm^2)	FF (%)	Eff (%)
$CdCl_2$	845	24	76	15
$ZnCl_2$	817	23.6	64.5	12.4
$MgCl_2$	776	23.9	61.3	11.4
NaCl	746	22.6	65.3	11.0
CuCl	637	22.2	57.6	8.2
KCl	685	23.0	49.9	7.9

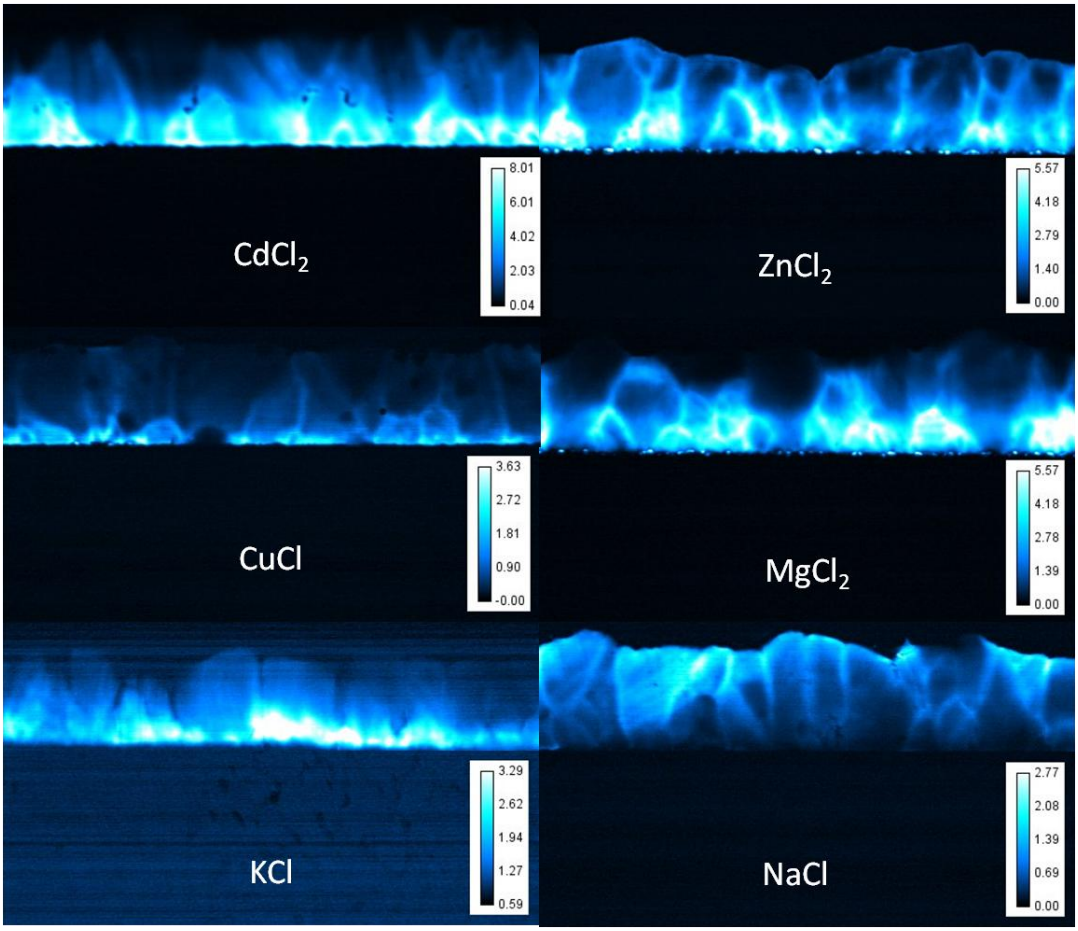

Figure D.2 EBIC comparison of six different Cl-based heat treatments; the standard treatment ($CdCl_2$) is compared to less toxic Cl salts. Currents are measured in nA.

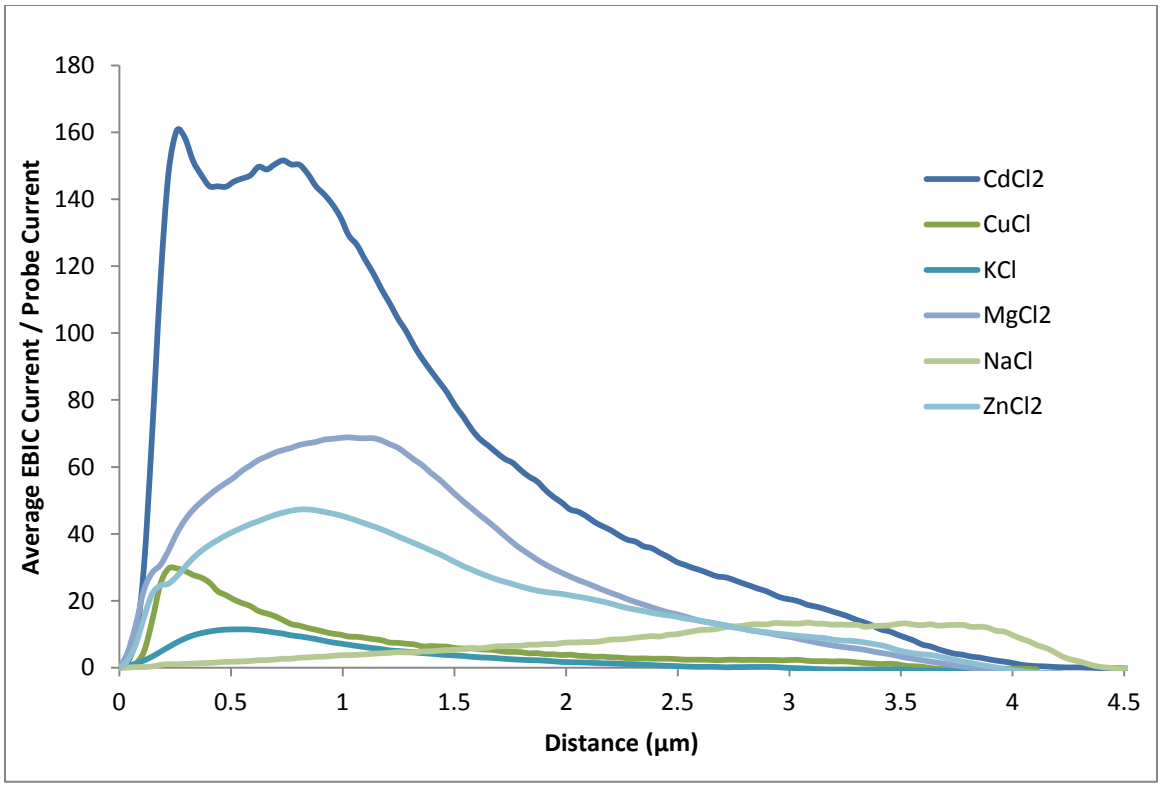

Figure D.3 The EBIC average line profiles of all six samples. The zero distance marks where the CdS ends and the CdTe begins.

REFERENCES

(1) Total Primary Energy Consumption http://www.eia.gov/cfapps/ipdbproject/IEDIndex3.cfm?tid=44&pid=44&aid=2 (accessed Sep 18, 2013).

(2) How much energy does a person use in a year? http://www.eia.gov/tools/faqs/faq.cfm?id=85&t=1 (accessed Oct 14, 2014).

(3) Shah, A.; Torres, P.; Tscharner, R.; Wyrsch, N.; Keppner, H. Photovoltaic Technology: The Case for Thin-Film Solar Cells. *Science (80-.).* **1999**, *285*, 692–698.

(4) Cusano, D. A. CdTe Solar Cells and Photovoltaic Heterojunctions in II–VI Compounds. *Solid-State Electronics*, 1963, *6*, 217–218.

(5) Swafford, L.; Rosenthal, S. J. Molecular Nanoelectronics. In; Reed, M. A.; Lee, T., Eds.; American Scientific Publishers, 2003.

(6) Nozik, A. . Quantum Dot Solar Cells. *Physica E: Low-dimensional Systems and Nanostructures*, 2002, *14*, 115–120.

(7) Abou-Ras, D.; Dietrich, J.; Kavalakkatt, J.; Nichterwitz, M.; Schmidt, S. S.; Koch, C. T.; Caballero, R.; Klaer, J.; Rissom, T. Analysis of Cu(In,Ga)(S,Se)2 Thin-Film Solar Cells by Means of Electron Microscopy. *Sol. Energy Mater. Sol. Cells* **2011**, *95*, 1452–1462.

(8) Schreuder, M. A.; Gosnell, J. D.; Smith, N. J.; Warnement, M. R.; Weiss, S. M.; Rosenthal, S. J. Encapsulated White-Light CdSe Nanocrystals as Nanophosphors for Solid-State Lighting. *Journal of Materials Chemistry*, 2008, *18*, 970.

(9) Bowers, M. J.; McBride, J. R.; Rosenthal, S. J. White-Light Emission from Magic-Sized Cadmium Selenide Nanocrystals. *J. Am. Chem. Soc.* **2005**, *127*, 15378–15379.

(10) Rosson, T. E.; Claiborne, S. M.; McBride, J. R.; Stratton, B. S.; Rosenthal, S. J. Bright White Light Emission from Ultrasmall Cadmium Selenide Nanocrystals. *J. Am. Chem. Soc.* **2012**, *134*, 8006–8009.

(11) Ng, A.; Poplawsky, J. D.; Li, C.; Pennycook, S. J.; Rosenthal, S. J. Direct Electronic Property Imaging of a Nanocrystal-Based Photovoltaic Device by Electron Beam-Induced Current via Scanning Electron Microscopy. *J. Phys. Chem. Lett.* **2014**, *5*, 856–860.

(12) Rosenthal, S. J.; Chang, J. C.; Kovtun, O.; McBride, J. R.; Tomlinson, I. D. Biocompatible Quantum Dots for Biological Applications. *Chemistry and Biology*, 2011, *18*, 10–24.

(13) Chang, J. C.; Rosenthal, S. J. Visualization of Lipid Raft Membrane Compartmentalization in Living RN46A Neuronal Cells Using Single Quantum Dot Tracking. *ACS Chem. Neurosci.* **2012**, *3*, 737–743.

(14) Klimov, V. I.; Mikhailovsky, A. A.; Xu, S.; Malko, A.; Hollingsworth, J. A.; Leatherdale, C. A.; Eisler, H.-J.; Bawendi, M. G. Optical Gain and Stimulated Emission in Nanocrystal Quantum Dots. *Science (80-.).* **2000**, *290*, 314–317.

(15) Loss, D.; DiVincenzo, D. P. Quantum Computation with Quantum Dots. *Physical Review A*, 1998, *57*, 120–126.

(16) De Rinaldis, S.; D'Amico, I.; Biolatti, E.; Rinaldi, R.; Cingolani, R.; Rossi, F. Intrinsic Exciton-Exciton Coupling in GaN-Based Quantum Dots: Application to Solid-State Quantum Computing. *Physical Review B*, 2002, *65*.

(17) Xiong, Y.; Wiley, B. J.; Xia, Y. Nanocrystals with Unconventional Shapes--a Class of Promising Catalysts. *Angew. Chem. Int. Ed. Engl.* **2007**, *46*, 7157–7159.

(18) Chen, J.; Lim, B.; Lee, E. P.; Xia, Y. Shape-Controlled Synthesis of Platinum Nanocrystals for Catalytic and Electrocatalytic Applications. *Nano Today*, 2009, *4*, 81–95.

(19) Rosenthal, S. J.; McBride, J.; Pennycook, S. J.; Feldman, L. C. Synthesis, Surface Studies, Composition and Structural Characterization of CdSe, Core/shell and Biologically Active Nanocrystals. *Surface Science Reports*, 2007, *62*, 111–157.

(20) Stolle, C. J.; Harvey, T. B.; Korgel, B. A. Nanocrystal Photovoltaics: A Review of Recent Progress. *Curr. Opin. Chem. Eng.* **2013**, *2*, 160–167.

(21) Kramer, I. J.; Sargent, E. H. Colloidal Quantum Dot Photovoltaics: A Path Forward. *ACS Nano*, 2011, *5*, 8506–8514.

(22) Alivisatos, A. P.; Gu, W.; Larabell, C. Quantum Dots as Cellular Probes. *Annu. Rev. Biomed. Eng.* **2005**, *7*, 55–76.

(23) Alivisatos, a P. Perspectives on the Physical Chemistry of Semiconductor Nanocrystals. *J. Phys. Chem.* **1996**, *100*, 13226–13239.

(24) Nozik, A. J. Quantum Dot Solar Cells. In *Physica E: Low-Dimensional Systems and Nanostructures*; 2002; Vol. 14, pp. 115–120.

(25) Chuang, C.-H. M.; Brown, P. R.; Bulović, V.; Bawendi, M. G. Improved Performance and Stability in Quantum Dot Solar Cells through Band Alignment Engineering. *Nat. Mater.* **2014**, *13*, 1–6.

(26) Saunders, B. R.; Turner, M. L. Nanoparticle-Polymer Photovoltaic Cells. *Advances in Colloid and Interface Science*, 2008, *138*, 1–23.

(27) Huynh, W. U.; Dittmer, J. J.; Alivisatos, A. P. Hybrid Nanorod-Polymer Solar Cells. *Science* **2002**, *295*, 2425–2427.

(28) Sun, B.; Greenham, N. C. Improved Efficiency of Photovoltaics Based on CdSe Nanorods and poly(3-Hexylthiophene) Nanofibers. *Phys. Chem. Chem. Phys.* **2006**, *8*, 3557–3560.

(29) Huynh, W.; Dittmer, J.; Teclemariam, N.; Milliron, D.; Alivisatos, A.; Barnham, K. Charge Transport in Hybrid Nanorod-Polymer Composite Photovoltaic Cells. *Physical Review B*, 2003, *67*.

(30) Huynh, W.; Dittmer, J.; Libby, W.; Whiting, G.; Alivisatos, a. Controlling the Morphology of Nanocrystal Polymer Composites for Solar Cells. *Adv. Funct. Mater.* **2003**, *13*, 73–79.

(31) Yu, D.; Wang, C.; Guyot-Sionnest, P. N-Type Conducting CdSe Nanocrystal Solids. *Science* **2003**, *300*, 1277–1280.

(32) Pattantyus-Abraham, A. G.; Kramer, I. J.; Barkhouse, A. R.; Wang, X.; Konstantatos, G.; Debnath, R.; Levina, L.; Raabe, I.; Nazeeruddin, M. K.; Grätzel, M.; *et al.* Depleted-Heterojunction Colloidal Quantum Dot Solar Cells. *ACS Nano* **2010**, *4*, 3374–3380.

(33) Barkhouse, D. A. R.; Debnath, R.; Kramer, I. J.; Zhitomirsky, D.; Pattantyus-Abraham, A. G.; Levina, L.; Etgar, L.; Grätzel, M.; Sargent, E. H. Depleted Bulk Heterojunction Colloidal Quantum Dot Photovoltaics. *Adv. Mater.* **2011**, *23*, 3134–3138.

(34) Ning, Z.; Voznyy, O.; Pan, J.; Hoogland, S.; Adinolfi, V.; Xu, J.; Li, M.; Kirmani, A. R.; Sun, J.; Minor, J.; *et al.* Air-Stable N-Type Colloidal Quantum Dot Solids. *Nat. Mater.* **2014**, *13*, 4–10.

(35) Lan, X.; Masala, S.; Sargent, E. H. Charge-Extraction Strategies for Colloidal Quantum Dot Photovoltaics. *Nat. Mater.* **2014**, *13*, 233–240.

(36) Maraghechi, P.; Labelle, A. J.; Kirmani, A. R.; Lan, X.; Adachi, M. M.; Thon, S. M.; Hoogland, S.; Lee, A.; Ning, Z.; Fischer, A.; *et al.* The Donor-Supply Electrode

Enhances Performance in Colloidal Quantum Dot Solar Cells. *ACS Nano* **2013**, *7*, 6111–6116.

(37) Mor, G. K.; Shankar, K.; Paulose, M.; Varghese, O. K.; Grimes, C. A. Use of Highly-Ordered TiO(2) Nanotube Arrays in Dye-Sensitized Solar Cells. *Nano Lett.* **2006**, *6*, 215–218.

(38) Jennings, J. R.; Ghicov, A.; Peter, L. M.; Schmuki, P.; Walker, A. B. Dye-Sensitized Solar Cells Based on Oriented TiO2 Nanotube Arrays: Transport, Trapping, and Transfer of Electrons. *J. Am. Chem. Soc.* **2008**, *130*, 13364–13372.

(39) Kuang, D.; Brillet, J.; Chen, P.; Takata, M.; Uchida, S.; Miura, H.; Sumioka, K.; Zakeeruddin, S. M.; Grätzel, M. Application of Highly Ordered TiO2 Nanotube Arrays in Flexible Dye-Sensitized Solar Cells. *ACS Nano* **2008**, *2*, 1113–1116.

(40) Sun, W. T.; Yu, A.; Pan, H. Y.; Gao, X. F.; Chen, Q.; Peng, L. M. CdS Quantum Dots Sensitized TiO2 Nanotube-Array Photoelectrodes. *J. Am. Chem. Soc.* **2008**, *130*, 1124–1125.

(41) Kongkanand, A.; Tvrdy, K.; Takechi, K.; Kuno, M.; Kamat, P. V. Quantum Dot Solar Cells. Tuning Photoresponse through Size and Shape Control of CdSe-TiO2 Architecture. *J. Am. Chem. Soc.* **2008**, *130*, 4007–4015.

(42) Kang, Q.; Liu, S.; Yang, L.; Cai, Q.; Grimes, C. A. Fabrication of PbS Nanoparticle-Sensitized TiO2 Nanotube Arrays and Their Photoelectrochemical Properties. *ACS Appl. Mater. Interfaces* **2011**, *3*, 746–749.

(43) Gong, D.; Grimes, C. A.; Varghese, O. K.; Hu, W.; Singh, R. S.; Chen, Z.; Dickey, E. C. Titanium Oxide Nanotube Arrays Prepared by Anodic Oxidation. *Journal of Materials Research*, 2001, *16*, 3331–3334.

(44) Prakasam, H. E.; Shankar, K.; Paulose, M.; Varghese, O. K.; Grimes, C. A. A New Benchmark for TiO2 Nanotube Array Growth by Anodization. *J. Phys. Chem. C* **2007**, *111*, 7235–7241.

(45) Williams, D. B.; Carter, C. B. *Transmission Electron Microscopy: A Textbook for Materials Science*; 2009; Vol. V1-V4, p. 760.

(46) De Broglie, L. Recherches Sur La Théorie Des Quanta. *Ann. la Fond. Louis Broglie* **1992**, *17*.

(47) Bunker, K. L.; Garcia, R.; Kennedy, T. J.; Stark, T. J.; Russell, P. E. Sample Preparation of Commercial Multiple Quantum Well Laser Diodes for Structural,

Compositional and Electrical Analysis in a Scanning Transmission Electron Microscope. **2004**.

(48) Erni, R. *Aberration-Corrected Imaging in Transmission Electron Microscopy*; IMPERIAL COLLEGE PRESS, 2010.

(49) Krivanek, O. L.; Nellist, P. D.; Dellby, N.; Murfitt, M. F.; Szilagyi, Z. Towards Sub-0.5 ?? Electron Beams. In *Ultramicroscopy*; 2003; Vol. 96, pp. 229–237.

(50) Pennycook, Stephen J., Nellist, P. D. (Eds. . *Scanning Transmission Electron Microscopy*; 2011; p. 762.

(51) Melngailis, J. Focused Ion Beam Technology and Applications. *Journal of Vacuum Science & Technology B: Microelectronics and Nanometer Structures*, 1987, *5*, 469.

(52) Harriott, L. R. Integrated Circuit Repair Using Focused Ion Beam Milling. *Journal of Vacuum Science & Technology B: Microelectronics and Nanometer Structures*, 1986, *4*, 181.

(53) Utke, I.; Hoffmann, P.; Melngailis, J. Gas-Assisted Focused Electron Beam and Ion Beam Processing and Fabrication. *Journal of Vacuum Science & Technology B: Microelectronics and Nanometer Structures*, 2008, *26*, 1197.

(54) Volkert, C. A.; Minor, A. M. Focused Ion Beam Microscopy and Micromachining. *MRS Bulletin*, 2007, *32*, 389–399.

(55) Giannuzzi, L. A.; Stevie, F. A. *Introduction to Focused Ion Beams: Instrumentation, Theory, Techniques and Practice*; 2005; pp. 1–357.

(56) Randolph, S. J.; Fowlkes, J. D.; Rack, P. D. Focused, Nanoscale Electron-Beam-Induced Deposition and Etching. *Critical Reviews in Solid State and Materials Sciences*, 2006, *31*, 55–89.

(57) Wang, S.; Sun, Y.-M.; Wang, Q.; White, J. M. Electron-Beam Induced Initial Growth of Platinum Films Using Pt(PF[sub 3])[sub 4]. *Journal of Vacuum Science & Technology B: Microelectronics and Nanometer Structures*, 2004, *22*, 1803.

(58) Giannuzzi, L. A.; Stevie, F. A. A Review of Focused Ion Beam Milling Techniques for TEM Specimen Preparation. *Micron* **1999**, *30*, 197–204.

(59) Hanoka, J. I.; Bell, R. O. Electron-Beam-Induced Currents in Semiconductors. *Annu. Rev. Mater. Sci.* **1981**, *11*, 353–380.

(60) Donolato, C. Spatial Resolution of SEM-EBIC Images. *Solid. State. Electron.* **1979**, *22*, 797–799.

(61) Leamy, H. J. Charge Collection Scanning Electron Microscopy. *J. Appl. Phys.* **1982**, *53*.

(62) Bresse, J.-F. Quantitative Investigations in Semiconductor Devices by Electron Beam Induced Current Mode: A Review. *Scanning Electron Microsc.* **1982**, 1487–1500.

(63) Xi, L.; Lam, Y. M. Controlling Growth of CdSe Nanowires through Ligand Optimization. *Chem. Mater.* **2009**, *21*, 3710–3718.

(64) Jönsson, S. K. M.; Birgerson, J.; Crispin, X.; Greczynski, G.; Osikowicz, W.; Denier van der Gon, A. W.; Salaneck, W. R.; Fahlman, M. The Effects of Solvents on the Morphology and Sheet Resistance in poly(3,4-Ethylenedioxythiophene)-Polystyrenesulfonic Acid (PEDOT-PSS) Films. *Synth. Met.* **2003**, *139*, 1–10.

(65) Ip, A. H.; Labelle, A. J.; Sargent, E. H. Efficient, Air-Stable Colloidal Quantum Dot Solar Cells Encapsulated Using Atomic Layer Deposition of a Nanolaminate Barrier. *Appl. Phys. Lett.* **2013**, *103*.

(66) Koleilat, G. I.; Kramer, I. J.; Wong, C. T. O.; Thon, S. M.; Labelle, A. J.; Hoogland, S.; Sargent, E. H. Folded-Light-Path Colloidal Quantum Dot Solar Cells. *Sci. Rep.* **2013**, *3*, 5.

(67) Xu, T.; Qiao, Q. Conjugated Polymer–inorganic Semiconductor Hybrid Solar Cells. *Energy & Environmental Science*, 2011, *4*, 2700.

(68) Dayal, S.; Reese, M. O.; Ferguson, A. J.; Ginley, D. S.; Rumbles, G.; Kopidakis, N. The Effect of Nanoparticle Shape on the Photocarrier Dynamics and Photovoltaic Device Performance of Poly(3-hexylthiophene):CdSe Nanoparticle Bulk Heterojunction Solar Cells. *Adv. Funct. Mater.* **2010**, *20*, 2629–2635.

(69) Albero, J.; Martínez-Ferrero, E.; Ajuria, J.; Waldauf, C.; Pacios, R.; Palomares, E. Photo-Induced Electron Recombination Dynamics in CdSe/P3HT Hybrid Heterojunctions. *Phys. Chem. Chem. Phys.* **2009**, *11*, 9644–9647.

(70) Noone, K. M.; Subramaniyan, S.; Zhang, Q.; Cao, G.; Jenekhe, S. A.; Ginger, D. S. Photoinduced Charge Transfer and Polaron Dynamics in Polymer and Hybrid Photovoltaic Thin Films: Organic vs Inorganic Acceptors. *J. Phys. Chem. C* **2011**, *115*, 24403–24410.

(71) Everhart, T. E.; Wells, O. C.; Matta, R. K. Evaluation of Passivated Integrated Circuits Using the Scanning Electron Microscope. *Journal of The Electrochemical Society*, 1964, *111*, 929.

(72) Pennycook, S. J. Investigation of the Electronic Effects of Dislocations by Stem. *Ultramicroscopy*, 1981, *7*, 99–104.

(73) Garnett, E. C.; Brongersma, M. L.; Cui, Y.; McGehee, M. D. Nanowire Solar Cells. *Annual Review of Materials Research*, 2011, *41*, 269–295.

(74) Reuter, P.; Rath, T.; Fischereder, A.; Trimmel, G.; Hadley, P. Electron Beam-Induced Current (EBIC) in Solution-Processed Solar Cells. *Scanning* **2011**, *33*, 1–6.

(75) Chesarek, W.; Mitchell, K.; Mason, A.; Fabick, L. EBIC Analysis of CuInSe2 Devices. *Sol. Cells* **1988**, *24*, 263–270.

(76) Li, C.; Poplawsky, J.; Wu, Y.; Lupini, A. R.; Mouti, A.; Leonard, D. N.; Paudel, N.; Jones, K.; Yin, W.; Al-Jassim, M.; *et al.* From Atomic Structure to Photovoltaic Properties in CdTe Solar Cells. *Ultramicroscopy* **2013**, *134*, 113–125.

(77) Kranz, L.; Gretener, C.; Perrenoud, J.; Schmitt, R.; Pianezzi, F.; La Mattina, F.; Blösch, P.; Cheah, E.; Chirilă, A.; Fella, C. M.; *et al.* Doping of Polycrystalline CdTe for High-Efficiency Solar Cells on Flexible Metal Foil. *Nat. Commun.* **2013**, *4*, 2306.

(78) Lang, J. R.; Faucher, J.; Tomasulo, S.; Nay Yaung, K.; Larry Lee, M. Comparison of GaAsP Solar Cells on GaP and GaP/Si. *Appl. Phys. Lett.* **2013**, *103*.

(79) Yacobi, B. G.; Holt, D. B. Cathodoluminescence Scanning Electron Microscopy of Semiconductors. *J. Appl. Phys.* **1986**, *59*.

(80) HOLT, D. B.; NAPCHAN, E. QUANTITATION OF SEM EBIC AND CL SIGNALS USING MONTE-CARLO ELECTRON-TRAJECTORY SIMULATIONS. *Scanning* **1994**, *16*, 78–86.

(81) Greenham, N.; Peng, X.; Alivisatos, A. Charge Separation and Transport in Conjugated-Polymer/semiconductor-Nanocrystal Composites Studied by Photoluminescence Quenching and Photoconductivity. *Physical Review B*, 1996, *54*, 17628–17637.

(82) Kamat, P. V. Quantum Dot Solar Cells. Semiconductor Nanocrystals as Light Harvesters. *J. Phys. Chem. C* **2008**, *112*, 18737–18753.

(83) Nozik, A. J.; Beard, M. C.; Luther, J. M.; Law, M.; Ellingson, R. J.; Johnson, J. C. Semiconductor Quantum Dots and Quantum Dot Arrays and Applications of

Multiple Exciton Generation to Third-Generation Photovoltaic Solar Cells. *Chem. Rev.* **2010**, *110*, 6873–6890.

(84) Hines, M. A.; Scholes, G. D. Colloidal PbS Nanocrystals with Size-Tunable Near-Infrared Emission: Observation of Post-Synthesis Self-Narrowing of the Particle Size Distribution. *Adv. Mater.* **2003**, *15*, 1844–1849.

(85) Poplawsky, J. D.; Paudel, N. R.; Li, C.; Parish, C. M.; Leonard, D.; Yan, Y.; Pennycook, S. J. Direct Imaging of Cl- and Cu-Induced Short-Circuit Efficiency Changes in CdTe Solar Cells. *Adv. Energy Mater.* **2014**, n/a – n/a.

(86) O'Regan, B.; Grätzel, M. A Low-Cost, High-Efficiency Solar Cell Based on Dye-Sensitized Colloidal TiO2 Films. *Nature*, 1991, *353*, 737–740.

(87) Buonsanti, R.; Carlino, E.; Giannini, C.; Altamura, D.; De Marco, L.; Giannuzzi, R.; Manca, M.; Gigli, G.; Cozzoli, P. D. Hyperbranched Anatase TiO2 Nanocrystals: Nonaqueous Synthesis, Growth Mechanism, and Exploitation in Dye-Sensitized Solar Cells. *J. Am. Chem. Soc.* **2011**, *133*, 19216–19239.

(88) Liu, B.; Aydil, E. S. Growth of Oriented Single-Crystalline Rutile TiO 2 Nanorods on Transparent Conducting Substrates for Dye-Sensitized Solar Cells. *J. Am. Chem. Soc.* **2009**, *131*, 3985–3990.

(89) Adachi, M.; Murata, Y.; Takao, J.; Jiu, J.; Sakamoto, M.; Wang, F. Highly Efficient Dye-Sensitized Solar Cells with a Titania Thin-Film Electrode Composed of a Network Structure of Single-Crystal-like TiO2 Nanowires Made by the "Oriented Attachment" Mechanism. *J. Am. Chem. Soc.* **2004**, *126*, 14943–14949.

(90) Ohsaki, Y.; Masaki, N.; Kitamura, T.; Wada, Y.; Okamoto, T.; Sekino, T.; Niihara, K.; Yanagida, S. Dye-Sensitized TiO2 Nanotube Solar Cells: Fabrication and Electronic Characterization. *Phys. Chem. Chem. Phys.* **2005**, *7*, 4157–4163.

(91) Wrenn, T.; McBride, J. R.; Smith, N. J.; Rosenthal, S. J. *Has the Sun Set on Quantum Dot-Sensitized Solar Cells?*; 2015.

(92) Peng, Z. A.; Peng, X. Formation of High-Quality CdTe, CdSe, and CdS Nanocrystals Using CdO as Precursor. *J. Am. Chem. Soc.* **2001**, *123*, 183–184.

(93) Mironov, V. S.; Kim, J. K.; Park, M.; Lim, S.; Cho, W. K. Comparison of Electrical Conductivity Data Obtained by Four-Electrode and Four-Point Probe Methods for Graphite-Based Polymer Composites. *Polym. Test.* **2007**, *26*, 547–555.

(94) Reguer, A.; Bedu, F.; Tonneau, D.; Dallaporta, H.; Prestigiacomo, M.; Houel, A.; Sudraud, P. Structural and Electrical Studies of Conductive Nanowires Prepared

by Focused Ion Beam Induced Deposition. *J. Vac. Sci. Technol. B Microelectron. Nanom. Struct.* **2008**, *26*, 175.

(95) Walton, A. S.; Allen, C. S.; Critchley, K.; Górzny, M. Ł.; McKendry, J. E.; Brydson, R. M. D.; Hickey, B. J.; Evans, S. D. Four-Probe Electrical Transport Measurements on Individual Metallic Nanowires. *Nanotechnology* **2007**, *18*, 065204.

(96) Spoddig, D.; Schindler, K.; Rödiger, P.; Barzola-Quiquia, J.; Fritsch, K.; Mulders, H.; Esquinazi, P. Transport Properties and Growth Parameters of PdC and WC Nanowires Prepared in a Dual-Beam Microscope. *Nanotechnology* **2007**, *18*, 495202.

(97) Serway, R. A. *Principles of Physics*; 2nd ed.; Saunders College Pub: Fort Worth, 1998; p. 602.

(98) Major, J. D.; Treharne, R. E.; Phillips, L. J.; Durose, K. A Low-Cost Non-Toxic Post-Growth Activation Step for CdTe Solar Cells. *Nature* **2014**, *511*, 334–337.

(99) Paudel, N. R.; Yan, Y. Fabrication and Characterization of High-Efficiency CdTe-Based Thin-Film Solar Cells on Commercial SnO2:F-Coated Soda-Lime Glass Substrates. *Thin Solid Films* **2013**, *549*, 30–35.